PLANT SCIENCES

Mitochondrial ROS trigger interorganellular signaling and prime ER processes to establish enhanced plant immunity

Yang Yang[1,2], Yan Zhao[1], Wei Zhao[1], Yingqi Zhang[1], Hongmei Wang[1], Murray Grant[3], Patrick Schäfer[4], Yuling Meng[1], Weixing Shan[1]*

Reactive oxygen species (ROS) are key signaling molecules in plant development and immunity, but current understanding is primarily focused on apoplastic and chloroplastic ROS. Mitochondria are also a key source of intracellular ROS, yet their contribution to plant immunity is poorly characterized. Here, we studied mitochondrial ROS (mROS) function in plant-pathogen interactions, deploying genetically encoded sensors, assorted fluorescent markers, and genetic approaches to track mROS, specifically H_2O_2, dynamics and identify interorganelle contact sites. We unexpectedly found a mitochondria–endoplasmic reticulum (ER) ROS signal cascade functioning independently of apoplastic and chloroplastic ROS in plant immunity. mROS initiate immune responses induced by the oomycete pathogen *Phytophthora parasitica* and promote mitochondria-ER association. These enhanced mitochondria-ER membrane associations are required for transfer of mROS signals and initiation of extensive unfolded protein responses. We conclude that mROS transfer via mitochondria-ER membranes to the ER lumen is an underappreciated yet essential component in plant defense.

INTRODUCTION

Plants have developed a complex and efficient immune system to protect against a diversity of pathogens. This typically involves two core signaling pathways, pattern-triggered immunity (PTI) and effector-triggered immunity (ETI) (*1*). However, adapted pathogens have evolved effectors to suppress PTI and colonize plants. Consequently, plants have developed resistance proteins (R). These predominately intracellular proteins, known collectively as nucleotide-binding leucine-rich repeat receptors (NLRs), detect the presence of effectors, eliciting ETI. There is increasing evidence for interdependency between PTI and ETI for effective activation of immunity (*1*–*3*).

Reactive oxygen species (ROS) are key signaling molecules deployed across all kingdoms of life (*4*). In plants, ROS act both locally and systemically (i.e., a ROS wave) during biotic and abiotic stress responses (*5*). The vast majority of our understanding of ROS in plant immunity is, however, mainly predicated on apoplastic ROS (apROS) produced by the plasma membrane–localized NADPH (reduced form of nicotinamide adenine dinucleotide phosphate) (RBOH) oxidases, particularly RBOHD and RBOHF (*6*–*11*).

Despite apROS being of intense interest, multiple organelles are, in fact, sources for cytoplasmic ROS in plant cells including the endoplasmic reticulum (ER), peroxisomes and the cellular powerhouses, chloroplasts, and mitochondria (*5*). Chloroplast ROS (cpROS) also function in both pattern- and effector-triggered immunity (*12*–*14*). Mitochondrial ROS (mROS) production is increasingly considered as a primary mitochondrial function (*15*). mROS functions in inflammatory responses have received extensive attention in mammalian research (*16*). mROS have received some attention in plant signaling and immunity (*17*–*21*), yet a fundamental understanding of mROS function in plant immunity is lacking.

Organelle interactions are involved in diverse cellular processes, including lipid and ion transfer, signaling, and organelle division in animals and yeasts (*22*). ER and mitochondria exchange signals and lipids through physical linkages known as mitochondria-associated membranes (MAMs) (*23*, *24*). ER-to-mitochondria Ca^{2+} transfer through MAMs contributes to pathogenesis and pathophysiology in mammalian cells (*25*). However, the function of interorganellular signaling in plant-pathogen interaction is poorly understood.

As key signal molecules, ROS transport across membranes and function in cell-to-cell or organelle-to-organelle interactions (*22*, *26*). H_2O_2 is considered the major molecule in ROS translocation, mainly mediated by aquaporins, due to its relatively long half-life (milliseconds) (*5*). Chloroplast-to-nucleus H_2O_2 transport is activated by high light to enable photosynthetic control over gene expression (*26*). Whether mitochondria-to-ER ROS transfer functions as a signaling cascade and plays a role in plant-pathogen interaction remains unknown.

Mitochondrial complex I on electron transport chain is one of the major mROS production sites (*27*). We previously found that the P-type pentatricopeptide repeat protein RTP7 (resistance to Phytophthora parasitica 7) participates in RNA splicing of the mitochondrial *nad7* transcript and negatively affects mROS accumulation through the complex I NAD7 subunit (*19*). The *rtp7*-mediated broad-spectrum resistance to pathogens with diverse lifestyles is dependent on its enhanced mROS levels.

Here, we show that mROS, specifically H_2O_2, is a major source of ER-ROS following *Phytophthora parasitica* infection and that its transfer into the ER matrix is crucial for activating ER process–related immune signaling, leading to enhanced disease resistance. High mROS levels promote MAM formation that recruit to *P. parasitica* haustoria and are associated with MAM-ROS and ER-ROS bursts, independent of cpROS and apROS. These findings define a mitochondria-MAM-ER ROS-signaling cascade with a vital role in the complex interorganelle dialog underpinning effective plant immunity.

[1]State Key Laboratory for Crop Stress Resistance and High-Efficiency Production and College of Agronomy, Northwest A&F University, Yangling, Shaanxi 712100, China. [2]State Key Laboratory for Crop Stress Resistance and High-Efficiency Production and College of Plant Protection, Northwest A&F University, Yangling, Shaanxi 712100, China. [3]School of Life Sciences, Gibbet Hill, University of Warwick, Coventry CV4 7AL, UK. [4]Institute of Phytopathology, Research Centre for BioSystems, Justus Liebig University, Giessen 35392, Germany.
*Corresponding author. Email: wxshan@nwafu.edu.cn

RESULTS

mROS contribute to immune responses at *P. parasitica* infection sites

We previously showed increased mROS levels in the *P. parasitica*–infected *Arabidopsis* root cells (*19*). Haustoria are specialized pathogen structures forming the interface that mediates plant-pathogen dialog (*28*). Taking advantage of a mitochondria-localized H_2O_2-specific biosensor (mt-roGFP2-Tsa2ΔC_R), we could analyze mROS levels of individual mitochondria inside infected cells. *P. parasitica* induced strong mROS bursts in the mitochondria surrounding haustoria compared with those distant from haustoria (Fig. 1, A and B), indicating that mROS might be important signals at the infection sites to initiate immune responses.

PTI is the first layer of plant immunity upon pathogen infection (*1*) and triggers mROS bursts (*19*). We noticed that apart from the strong mROS burst, flg22 treatment (a 22–amino acid immunoactivating peptide of bacterial flagellin) also triggered network-like ROS signals in *Arabidopsis* root cells, as revealed by 2,7-dichlorofluorescein diacetate (CM-H_2DCFDA, ROS) and MitoTracker Red (mitochondria) staining (fig. S1, A and B). Furthermore, *rtp7 Arabidopsis* mutants showed increased PTI-induced mROS bursts (*19*) and flg22-induced network-like ROS bursts (fig. S1, C and D), indicating that flg22 could induce network-like ROS bursts and that it might be related to mROS.

We then analyzed whether PTI-induced network-like ROS bursts depended on mitochondrial permeability transition pore (mPTP)–mediated mROS release. The higher level of mROS would be released through mPTP in mitochondrial membranes (*29*). We first analyzed whether mPTP could format and open in PTI or upon pathogen infection. The mPTP formation and opening induce decreased mitochondrial membrane potential ($\Delta\Psi$m) and mitochondrial swelling (*30*). We showed that *P. parasitica* infection or flg22 treatment reduced $\Delta\Psi$m (fig. S1E) and that mitochondria gathered around *P. parasitica* haustoria are bigger in size than that of uninfected cells (fig. S1E), indicating a potential role of mPTP formation and opening in plant immunity.

mPTP contains two inner mitochondrial membrane-localized components, ANTs (adenine nucleotide translocators) and CypD (cyclophilin D), and outer mitochondrial membrane (OMM)–localized VDAC (voltage-dependent anion channel) proteins (*29*). Bongkrekic acid (BA), an inhibitor of ANTs, inhibits mPTP opening in plant cells (*29*, *31*). Four of the *Arabidopsis VDAC* genes (*VDAC1*, *VDAC2*, *VDAC3*, and *VDAC4*) were identified, and their VDAC functions in mROS homeostasis were confirmed (*32*, *33*). Among these four *VDACs*, *AtVDAC3* expression is induced by bacterial infection, and it regulates plant resistance to bacterial pathogen *Pseudomonas syringae* (*33*, *34*). Therefore, we inhibited mPTP opening by BA treatment or knocking-out *VDAC3*. The mROS staining showed that BA treatment or *VDAC3* knocking out reduced flg22-induced network-like ROS levels (fig. S1, A to D), indicating mROS as the ROS source.

mROS trigger a mitochondria-ER ROS cascade independently of apROS

We further analyzed the localization of the network-like ROS. The network-like morphology suggested the distribution of this mROS-dependent ROS signals in ER. However, as PTI could induce ROS burst from multiple organelles and apoplast (*6*–*11*, *14*, *35*), to avoid potential influence of other ROS sources during PTI, we used MitoPQ, a specific mROS inducer of complex I without affection of normal oxidative phosphorylation (*36*) to directly trigger an mROS burst. The MitoPQ treatment of *Arabidopsis* Col-0–expressing ER-lumen–targeted cyan fluorescent protein (CFP) (ER-CFP), followed by DCF and MitoTracker Red staining, showed that MitoPQ could induce mROS (Fig. 1, C and D). The MitoPQ-triggered network-like ROS signals were associated with ER signals, while the solvent control of MitoPQ [0.01% dimethyl sulfoxide (DMSO)] did not trigger strong ROS signals (Fig. 1, C and D). Moreover, the ER-associated ROS signals around mitochondria were stronger than the ER-associated ROS signals more distant from mitochondria (Fig. 1, C and D), indicating that the network-like ROS induced by MitoPQ were related to ER-ROS. To rule out potential side effect of MitoPQ on ER and direct triggering of ER-ROS, we detected ER-ROS levels in *rtp7* mutants that showed stronger mROS production (*19*). We found that, apart from the stronger mROS signals, *rtp7* knock-out mutants also showed stronger ER-ROS signals compared with Col-0 (Fig. 1E). These results indicate that activation of mROS triggers ER-ROS bursts in *Arabidopsis*.

Genetically encoded biosensors provide better specificity and resolution for ROS detection than DCF staining (*37*). We therefore further confirmed that MitoPQ could trigger ER-ROS burst using ER-lumen–targeted redox sensor roGFP2 (ER-roGFP2) and Grx1-roGFP2iL (ER-Grx1-roGFP2iL), H_2O_2-specific sensor roGFP2-Tsa2ΔC_R (ER-roGFP2-Tsa2ΔC_R), and HyPer7 (ER-HyPer7) in *Nicotiana benthamiana* leaves (Fig. 1F and fig S2, A and B; see Materials and Methods for detailed descriptions). Moreover, MitoPQ-induced ER-ROS were also detected by ROS staining in *N. benthamiana* leaves (fig. S3).

As MitoPQ has not been used for confocal imaging of plant cells, we performed pilot experiments to optimize its use in planta. We determined that a MitoPQ concentration of 0.5 μM was sufficient to induce mROS bursts in *Arabidopsis* roots and *N. benthamiana* leaves without causing obvious cytotoxicity under our experimental conditions (fig. S4 and experimental details in Materials and Methods). We previously showed that virus-induced gene silencing (VIGS) of *NbRTP7* increased mROS levels (*19*). Both ROS biosensors and ROS staining assays revealed enhanced ER-ROS levels in *NbRTP7*-silenced *N. benthamiana* leaves (Fig. 1F and fig. S3). Together, these results indicate that activation of mROS results in ER-ROS bursts.

We next analyzed whether this mROS-induced ER-ROS burst was dependent on ROS transport of ER and mitochondria. ROS translocation is primarily mediated by aquaporins in ER membrane (*38*, *39*) and mPTP in mitochondrial membranes (*29*). Small basic intrinsic proteins (SIPs) are ER membrane–localized aquaporins (*40*, *41*). ROS staining in MitoPQ-treated *Arabidopsis sip1;1-1*, and *sip1;1-2* mutant roots showed reduced ER-ROS levels (fig. S5, A and B). Inactivating mPTP by BA (*29*) or knocking out *VDAC3* in MitoPQ-treated *Arabidopsis* roots significantly reduced MitoPQ-induced ER-ROS signals (fig. S5, C to E). These results indicate that the mROS-induced ER-ROS burst is dependent on ROS transport of mitochondria and ER.

As ER oxidoreductins (EROs) produce ROS in the ER-lumen as secondary products, arising from the formation and rearrangement of protein disulfide bonds (*38*), we examined whether mROS-induced ER-ROS are resulted from the activation of ER-ROS production in ER lumen. Two EROs (*ERO1* and *ERO2*) have been identified in *Arabidopsis* genome (*42*). MitoPQ treatment still induced ER-ROS in the *ERO*–knocking down *Arabidopsis* mutants

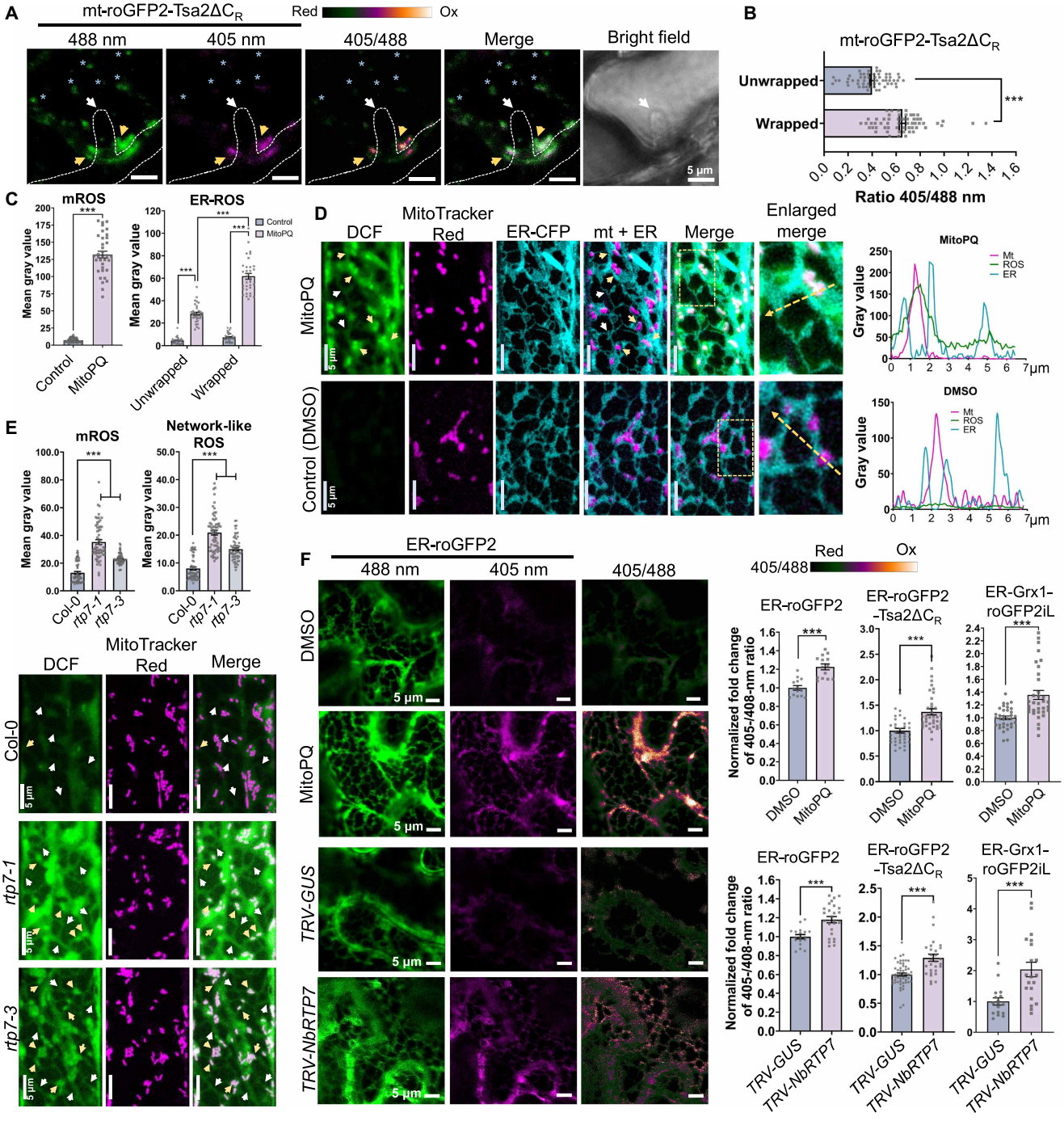

Fig. 1. mROS induce ER-ROS bursts. (**A** and **B**) Confocal microscopy of mROS around haustoria (A) and quantification (B). mROS were measured by expressing mt-roGFP2-Tsa2ΔC$_R$ in *N. benthamiana* leaves. Yellow arrows mark haustoria-wrapped mitochondria, and white arrows mark haustoria. Blue asterisks mark haustoria-unwrapped mitochondria. Scale bars, 5 μm (A). (**C** and **D**) Gray value analyses (C) and confocal microscopy analysis (D) of mROS and network-like ROS in root cells of a stable-transgenic *Arabidopsis* line expressing ER-CFP in the Col-0 upon 0.5-μM MitoPQ treatment for ~1 hour. 0.01% DMSO (v/v, control) is the MitoPQ solvent. Yellow arrows mark ER region around mitochondria (wrapped), and white arrows mark the ER region distant from mitochondria (unwrapped). Gray value plots show relative fluorescence along the dotted lines. Scale bars, 5 μm. (**E**) Confocal microscopy analysis (bottom) and gray value analyses (top) of mROS and network-like ROS in root cells of Col-0 and *rtp7* mutants. Yellow arrows mark the mROS signals, and white arrows mark the network-like ROS signals. Scale bars, 5 μm. (**F**) Confocal microscopy analysis of ER-lumen redox status in *N. benthamiana* leaves expressing *ER-roGFP2*, *ER-roGFP2-Tsa2ΔC$_R$*, and *ER-Grx1-roGFP2iL* upon MitoPQ treatment (top) and *TRV-NbRTP7* silencing (bottom). Scale bars, 5 μm. Bars are presented as the means ± SE. ROS were visualized via CM-H$_2$DCFDA (DCF; false-colored green), and mitochondria were marked with MitoTracker Red (false-colored magenta) [(D) and (E)]. Data points represent different mitochondria or ER regions from at least three biological repeats. Statistical significance was assessed by Brown-Forsythe analysis of variance (ANOVA) test with Dunnett's T3 post hoc test (E), two-way ANOVA with Tukey's post hoc test [ER-ROS in (C)], or two-tailed Student's *t* test [(B), mROS in (C), and (F)]. ***$P < 0.001$ and ns, not significant. All the experiments were repeated three times with similar results.

(*ero1-1*, *ero1-2*, *ero2*) (fig. S5, A and B), suggesting that the mROS-induced ER-ROS bursts are not associated with ROS production in ER-lumen. These results suggest that MitoPQ-induced ER-ROS depend on mROS transport.

apROS are the best characterized ROS signaling mechanism (*6*–*11*). To further exclude the possibility that mROS-induced ER-ROS bursts were apoplastically derived, we first assayed ER-ROS in the roots of *Arabidopsis rbohD*, *rbohD rbohF* (*rbohD/F*), and *rtp7 rbohD* double mutants and the *rtp7 rbohD rbohF* (*rtp7 rbohD/F*) triple mutant following MitoPQ treatment. The loss of *RBOHD* or *RBOHF* had no discernable effect on the MitoPQ-induced ER-ROS bursts (fig. S5, F and G), suggesting that mROS-induced ER-ROS may not derive from apoplastic sources. Collectively, these results consistently indicate that mROS-triggered mitochondria-ER ROS cascade is independent of apROS.

mROS promote MAM formation independently of mitochondria-ER ROS cascades

The mitochondrial outer membrane and ER membrane form MAMs that mediate their material and signal exchanges (*23*, *24*). To determine whether mROS affect their physical interactions and facilitate mitochondria-ER ROS cascade, we performed transmission electron microscopy on *Arabidopsis* roots. The results showed that mitochondria-ER association was enhanced in *rtp7* mutants (Fig. 2, A and C), and MitoPQ-treated *Arabidopsis* root cells similarly showed enhanced association of ER and mitochondria (Fig. 2, B and C). These results suggest that mROS activation promotes MAM formation.

To quantitatively monitor mitochondria-ER interactions in living cells, we adapted a split–green fluorescent protein (GFP)–based complementation assay (*43*, *44*) in *N. benthamiana* leaves (Fig. 2E and fig. S6, A and B). GFP was separated into two parts, comprising non-fluorescing $GFP_{\beta 11}$ and $GFP_{\beta 1-10}$ fragments. We fused the ER membrane–anchoring sequence with $GFP_{\beta 11}$ (ER-$GFP_{\beta 11}$) to tether it to the cytoplasmic surface of ER membranes. $GFP_{\beta 1-10}$ was then linked to the outer-mitochondrial-membrane (OMM) anchoring sequence (OMM-$GFP_{\beta 1-10}$) to tether it to the cytoplasmic surface of the OMM (Fig. 2E). Transient coexpression of different combinations of $GFP_{\beta 11}$, $GFP_{\beta 1-10}$, *ER-*$GFP_{\beta 11}$ and *OMM-*$GFP_{\beta 1-10}$ in *N. benthamiana* leaves, with ER-CFP and mt-RFP (red fluorescent protein) markers, indicated that only the *ER-*$GFP_{\beta 11}$ and *OMM-*$GFP_{\beta 1-10}$ combination could confer strong GFP fluorescence between mitochondria and ER (fig. S6, A and B, with experimental details in Materials and Methods), thus demonstrating specificity of the assay in plant cells. We quantified mitochondria-ER contacts using three parameters: total fluorescence intensity per cell, the percentage of cell area occupied by GFP fluorescence, and the total number of fluorescent foci ("spots") per cell (*43*). Split-GFP assays showed that mROS activation by MitoPQ treatment or *NbRTP7* silencing in *N. benthamiana*, increased MAM formation (Fig. 2, F and G). Moreover, direct measuring of the distance between ER and mitochondria in *N. benthamiana* leaves that express ER and mitochondria markers, revealed that MitoPQ treatment or *NbRTP7* silencing both enhanced ER-mitochondria association (Fig. 2D). Together, these results indicate that the split-GFP assay could be used for MAM detection and that the increased mROS levels promote MAM formation.

To further understand whether mROS-induced MAM formation is dependent on the mitochondria-ER ROS cascade, we first examined the effect of mROS release inhibition on MAM formation. The mPTP was blocked by silencing of *NbVDAC* or treating with mPTP inhibitor BA. BA treatment did not affect MitoPQ-induced MAM formation (fig. S7A), while *NbVDAC*-silencing reduced it (fig. S7B). Because VDAC not only is not only a key subunit of mPTP but also functions as a physical MAM linker (*45*), we hypothesize that VDAC might function as a key physical MAM linker in mROS-induced MAM formation.

To analyze whether mROS-induced MAM formation is related to *NbSIP*-mediated ER-ROS transport or *NbERO*-related ER-ROS production, we examined MAM formation in *TRV-NbSIP1/2* and *TRV-NbERO N. benthamiana* leaves upon MitoPQ-treatment. The silencing of *NbSIPs* and *NbERO* did not affect MitoPQ-induced MAM formation (fig. S7, B and C), indicating that mROS-induced MAM formation is not related to ER-ROS production or transport. Together, these results indicate that mROS-mediated MAM formation requires VDACs but is independent of either ROS transfer or ER-ROS production.

mROS promote MAM-ROS burst

As mROS promote MAM formation (Fig. 2) and mROS trigger ER-ROS (Fig. 1), we further investigated whether mROS induce the MAM-ROS burst. Because current ROS-staining methods do not provide sufficient resolution to quantify MAM-ROS at the ER-mitochondrial interface, we established a method in plant cells that adapted a rapamycin-inducible synthetic linker established for mammalian systems (*46*) to target genetically encoded redox sensors to MAMs (Fig. 3A). Linker function relies on the rapamycin-induced heterodimerization of the FKBP domain (FKBP) of human FKBP12 with the FKBP12 rapamycin-binding domain (FRB) of mammalian target of rapamycin (mTOR) (*46*).

We fused the ER-membrane–anchoring sequence to the GFP-tagged FRB domain (ER-GFP-FRB) to target it to the cytoplasmic surface of the ER membrane and linked the red fluorescent protein (RFP)–tagged FKBP domain with the OMM anchoring sequence of TOM70 (OMM-RFP-FKBP) to localize it to the cytoplasmic OMM surface (Fig. 3A). Upon addition of rapamycin, ER-GFP-FRB and OMM-RFP-FKBP are crosslinked and concentrated at contact sites of mitochondria and ER (Fig. 3A). By transient coexpression in *N. benthamiana* leaves, we showed that ER-GFP-FRB was targeted to network structures that colocalized with the ER-lumen marker ER-CFP (Fig. 3B). Rapamycin treatment induced formation of small ER-GFP-FRB dots that colocalized with OMM-RFP-FKBP (Fig. 3B). Quantitative analysis confirmed less colocalization of ER-GFP-FRB and ER-CFP and more colocalization of ER-GFP-FRB and OMM-RFP-FKBP (Fig. 3C). ER morphology remained unchanged during rapamycin treatment (Fig. 3B). The GFP protein was replaced by biosensors roGFP2-Tsa2ΔC_R or roGFP2 to track MAM-ROS.

By using this method, MitoPQ treatment or *NbRTP7* silencing in *N. benthamiana* both showed increased H_2O_2 levels at MAMs (Fig. 3D), indicating that increased mROS trigger MAM-ROS bursts.

P. parasitica–induced mROS initiate MAM formation around haustoria

We showed that mROS induced MAM formation without pathogen inoculation (Fig. 3). To place the mROS-induced MAM formation in a physiological context, we examined whether it occurred during immune responses. Because we previously found that mROS bursts were triggered by PTI (*19*) and mROS-induced MAM formation (Fig. 3D), we first analyzed whether PTI could induce MAM formation. flg22 treatment promoted MAM formation in *N. benthamiana*

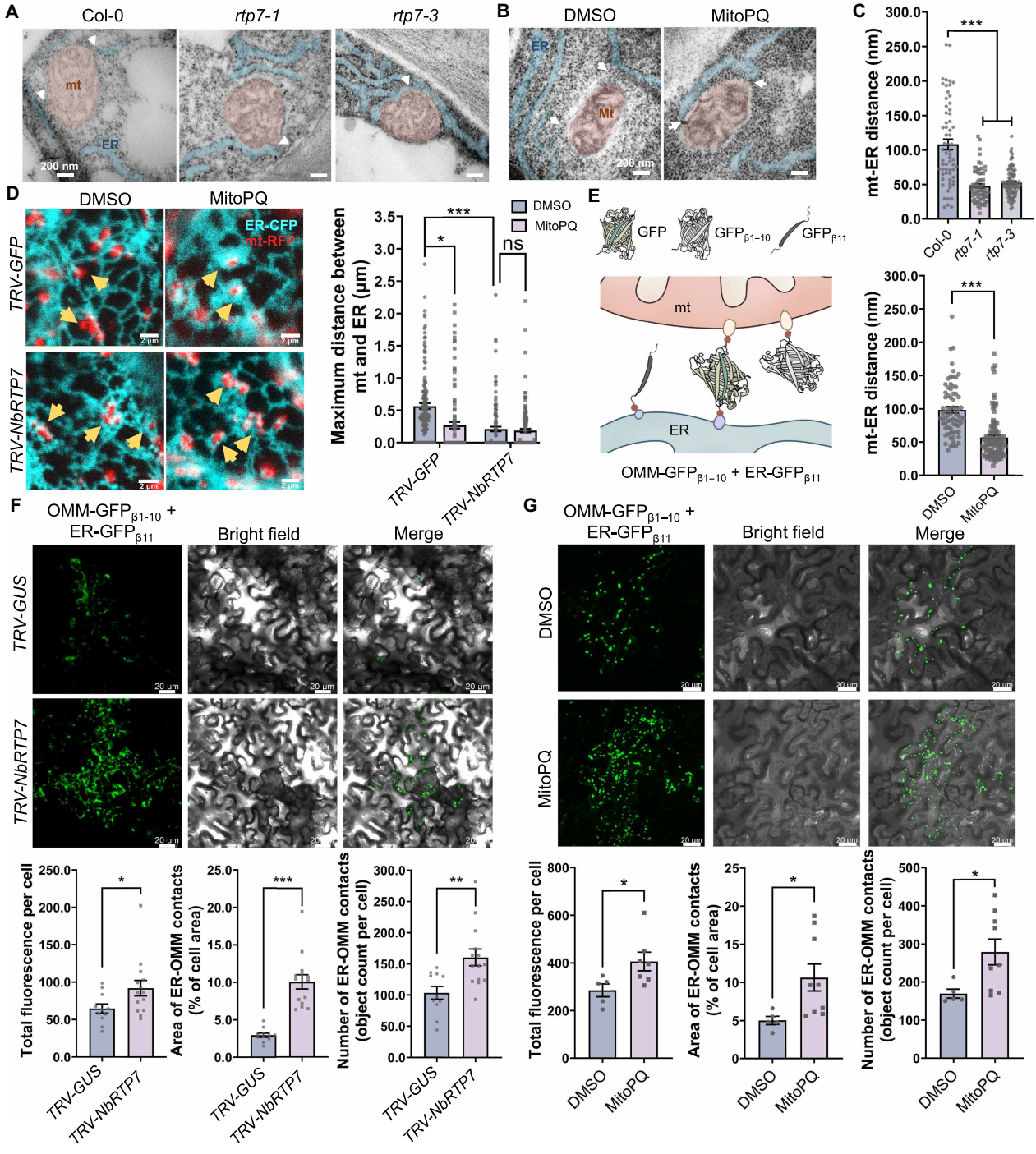

Fig. 2. mROS promote MAM formation. (**A** to **C**) Transmission electron microscopy to track ER and mitochondria interactions in *Arabidopsis rtp7* mutants (A), MitoPQ-treated Col-0 roots (B), and distance quantification (C). Mitochondria are marked in pink and ER in light blue. Scale bars, 200 nm. Data points represent the distance between ER and mitochondria from three biological repeats. (**D**) Confocal microscopy (left) and statistical analysis (right) of the maximum distance between mitochondria and ER in *TRV-NbRTP7* (*TRV-GFP* as control) and MitoPQ-treated (with 0.01% DMSO as mock control) *N. benthamiana* leaves. ER and mitochondria were marked by ER-CFP and mitochondria-targeted RFP (mt-RFP), respectively. Yellow arrows mark mitochondria around the ER. Leaves were treated with 500 nM MitoPQ for ~3 hours before imaging. Scale bars, 2 μm. Data points represent distances between different mitochondria to ER networks. (**E**) Schematic of split-GFP–based assay for detection of mitochondria-ER interactions by confocal microscopy. GFP was separated into two parts to receive nonfluorescing GFP$_{β11}$ and GFP$_{β1–10}$ fragments and targeted to the surface of the ER membrane (ER-GFP$_{β11}$) and outer mitochondria membrane (OMM-GFP$_{β1–10}$). (**F** and **G**) Confocal microscopy analysis of GFP fluorescence in *N. benthamiana* coexpressing *OMM-GFP$_{β1–10}$* and *ER-GFP$_{β11}$* in *NbRTP7*-silenced leaves (F) or upon MitoPQ treatment (G). Scale bars, 20 μm. Data points represent different cells from four biological repeats. All bars present the mean ± SE. Statistical significance was assessed by two-tailed Student's *t* test [(C), bottom, (F), and (G)], two-way ANOVA with Tukey's post hoc test (D) or one-way ANOVA with Dunn's post hoc test against Col-0 in (C) (top). **P* < 0.05, ***P* < 0.01, and ****P* < 0.001. All the experiments were repeated at least two times with similar results.

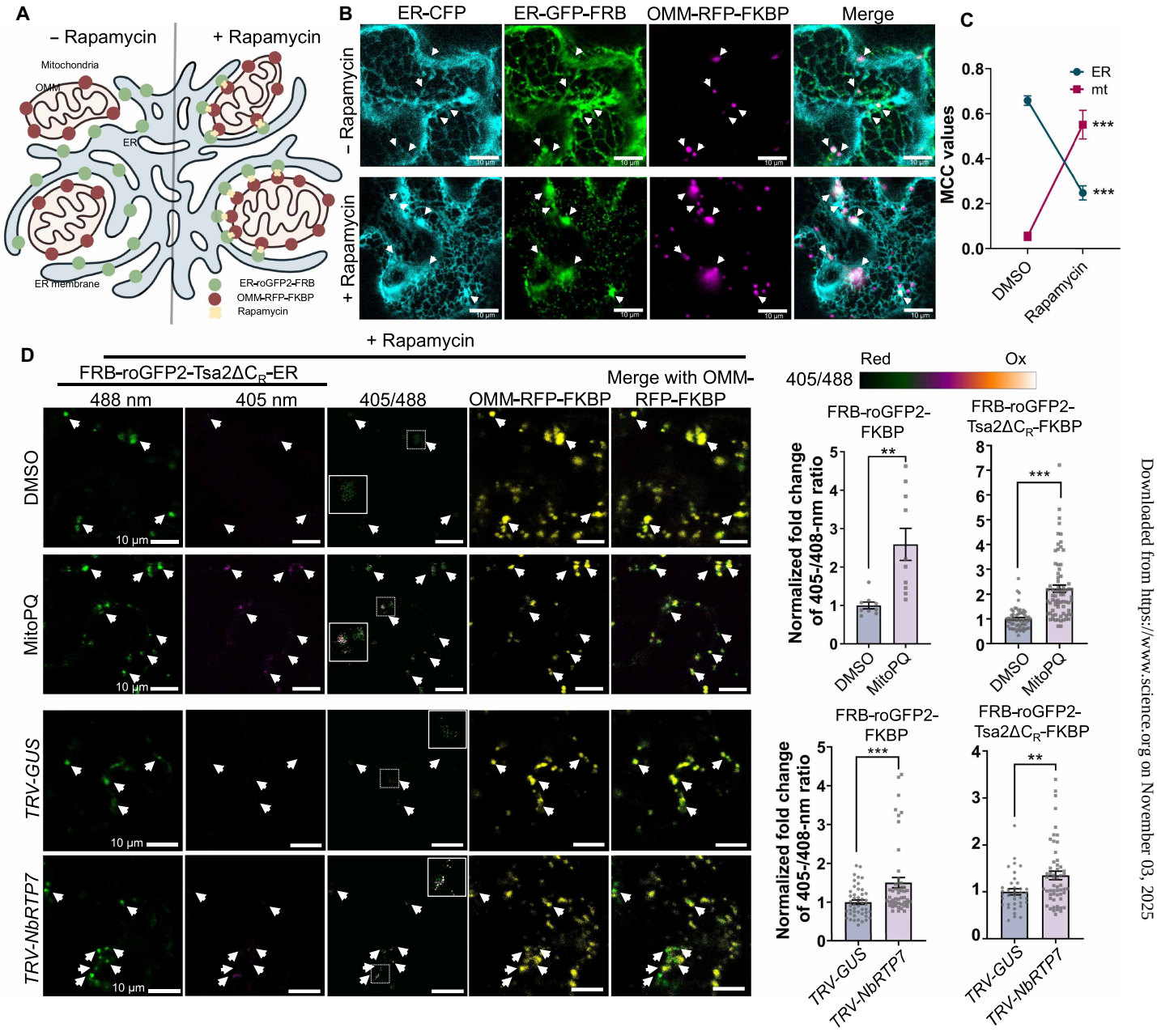

Fig. 3. mROS promote MAM-ROS. (**A**) Schematic for targeting ROS sensors to MAMs. Upon rapamycin treatment, mitochondria-ER interactions lead to the heterodimerization of the OMM-targeted FKBP domain fused to RFP (OMM-RFP-FKBP) with the ER-surface–targeted FRB domain fused to roGFP2 (ER-roGFP2-FRB), resulting in ER-GFP-FRB enrichment at organelle interaction sites trackable by confocal microscopy. GFP was replaced by roGFP2 sensors to detect MAM-ROS. (**B** and **C**) Rapamycin-inducible method relocalizes target proteins to MAMs. Colocalization (B) and quantification (C) of ER-GFP-FRB with OMM-RFP-FKBP and the organelle marker ER-CFP in *N. benthamiana* leaves. Colocalization between GFP signals with ER (ER) or mitochondria (mt) was performed by Manders colocalization coefficients (MCCs) using ImageJ. The white arrows mark mitochondria. Scale bars, 10 μm. Data points represent MCC values of different cells from three biological repeats. (**D**) Confocal microscopy analysis of MAM-ROS in *NbRTP7*-silenced and MitoPQ-treated *N. benthamiana* leaves. A 0.01% DMSO served as solvent control of MitoPQ treatment, and *TRV-GUS* was the control for *TRV-NbRTP7*. Rapamycin was applied 30 min before imaging. Scale bars, 10 μm. Dashed squares mark the enlarged inset images. All bars present the means ± SE. Statistical significance was assessed by two-tailed Student's *t* test (C and D). $^{**}P < 0.01$ and $^{***}P < 0.001$. All the experiments were repeated three times with similar results.

leaves, which was reduced by mROS scavengers MitoTEMPOL and NAC (*N*-acetyl-L-cysteine) (fig. S7, D and E), indicating that flg22 could trigger mROS-dependent MAM formation. These results indicate that PTI triggers mROS-dependent MAM formation.

Pathogens often induce organelle aggregation at infection sites (*47*–*49*). In our previous work in *Arabidopsis*, mitochondria were shown to be enriched around *P. parasitica* haustoria, which was further promoted in *rtp7* mutants, indicating that mROS might be related to this mitochondria aggregation around haustoria (Fig. 4A) (*19*). We also showed that ER was enriched around haustoria (*49*). Therefore, we investigated whether the aggregation of mitochondria and ER around haustoria could be observed simultaneously by coexpressing

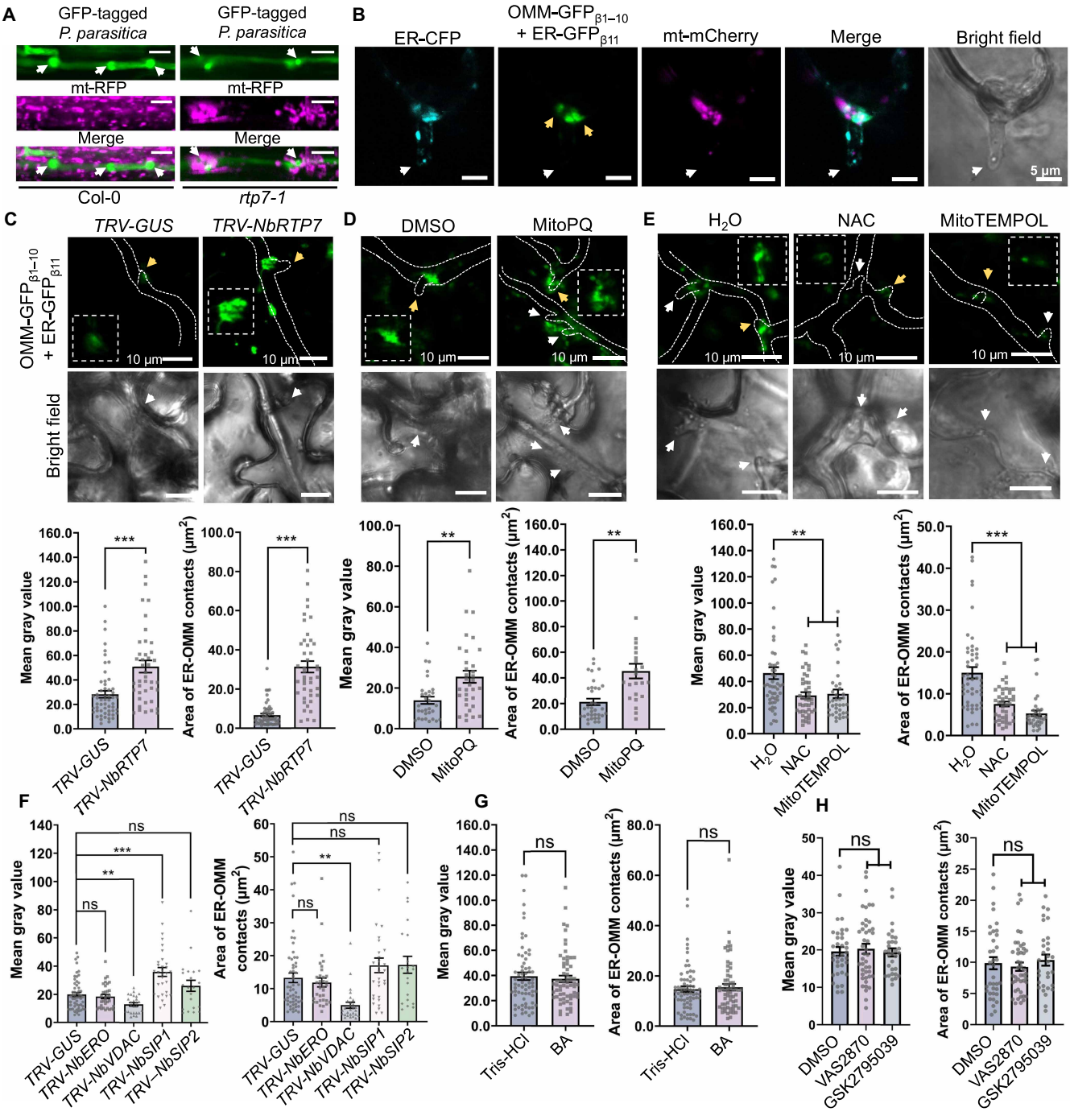

Fig. 4. mROS initiate MAM formation around haustoria. (**A**) Confocal microscopy of transgenic *Arabidopsis* roots stably expressing mt-RFP marker (mt-RFP, false-colored magenta) inoculated with GFP-tagged *P. parasitica* zoospores (false-colored green) for ~15 hours before imaging. The white arrows mark haustoria. Scale bars, 10 μm. (**B**) Confocal microscopy of mitochondria (mt-mCherry), ER (ER-CFP), and mitochondria-ER contact sites in *P. parasitica*–infected *N. benthamiana* leaves. Yellow arrows mark MAM sites, and white arrows mark the *P. parasitica* haustoria. Scale bars, 5 μm. The ER-CFP signals were enriched around haustoria with some puncta visible. The puncta-like GFP signals indicate MAM formation. (**C** to **E**) GFP fluorescence, mean gray values, and areas of mitochondria-ER contact sites in *P. parasitica*–infected *N. benthamiana* coexpressing *OMM-GFP*$_{\beta1-10}$ and *ER-GFP*$_{\beta11}$ in *NbRTP7*-silenced leaves (C), upon MitoPQ treatment (D), or upon NAC and MitoTEMPOL treatment (E). Scale bars, 10 μm. The dashed lines mark *P. parasitica* hyphae on focal plane. The arrows mark haustoria. The inset images are higher magnification of GFP signals around the yellow arrow marked haustoria. The puncta-like GFP signals indicate MAM formation. (**F** to **H**) Analysis of MAMs in *NbERO*-, *NbVDAC*-, *NbSIP1*-, and *NbSIP2*-silenced *N. benthamiana* leaf cells (F) or upon BA treatment (G) and RBOH inhibitor treatment (VAS2870 and GSK2795039) (H) in *P. parasitica*–infected leaves. Data points represent MAM signals around different haustoria from four biological repeats. Bars are presented as the means ± SE. Statistical significance was assessed by two-tailed Student's *t* test [(C), (D), and (G)] or one-way ANOVA with Dunn's post hoc test against control [(E), (F), and (H)]. $^{**}P < 0.01$ and $^{***}P < 0.001$ and ns, not significant. All the experiments were repeated at least two times with similar results.

ER-roGFP2-Tsa2ΔC$_R$ as an ER marker with OMM-localized RFP (*OMM-RFP*) in *N. benthamiana*, followed by *P. parasitica* inoculation. Punctate ER signals were observed on haustoria-wrapped ER and in ER near haustoria, while the uninfected cells showed well-organized network-like ER signals (fig. S8), indicating that the morphological structure of the ER was affected by *P. parasitica* infection. Mitochondria and ER enriched around haustoria, and their aggregation could be observed simultaneously around haustoria (fig. S8A), indicating the formation of MAM around haustoria.

We subsequently confirmed that MAM formed when mitochondria and ER aggregated around *P. parasitica* haustoria (Fig. 4B), as revealed by transient expression of ER-localized CFP (ER-CFP), mitochondria-localized mCherry (mt-mCherry), ER-GFP$_{\beta 11}$, and OMM-GFP$_{\beta 1-10}$ in *N. benthamiana* leaves. This MAM formation was further promoted by increased mROS following MitoPQ treatment or via *NbRTP7* silencing (Fig. 4, C and D) but was attenuated by mROS scavengers MitoTEMPOL and NAC (Fig. 4E). These data indicate that MAM formation around haustoria is dependent on pathogen-induced mROS bursts.

We showed that in the absence of *P. parasitica* infection, mROS-induced MAM-formation was independent of SIPs and EROs, and that VDACs might function as a physical MAM linker in mROS-induced MAM formation (Fig. 2 and fig. S7, A to E). In experiments examining *P. parasitica* infection, the results were similar to uninfected cells (Fig. 4, F and G), demonstrating that the MAM formation around haustoria is also VDAC dependent.

As RBOH-mediated apROS burst is key for plant immunity (*6*–*11*), we further analyzed whether it also regulates MAM formation around haustoria. Inhibiting RBOHs by DPI (diphenyleneiodonium chloride) at a concentration sufficient to inhibit the immunity-induced apROS burst (fig. S9A) did not affect MAM formation around haustoria (fig. S9B). Moreover, inhibiting RBOHs using the two more specific NOX (NADPH oxidase) inhibitors, VAS2870 (*50*) and GSK2795039 (*51*), did not affect MAM formation around haustoria (Fig. 4H). The concentration of VAS2870 and GSK2795039 were sufficient to inhibit the PTI-induced apROS burst (fig. S9, C and D) but did not affect the immunity-induced mROS burst (fig. S9E). The expression of *ER-GFP$_{\beta 11}$* and *OMM-GFP$_{\beta 1-10}$* in all split-GFP assay was confirmed (fig. S10). Collectively, these results indicated that the MAM formation around haustoria is initiated by pathogen-induced mROS bursts and independent of apROS.

mROS initiate mitochondria-MAM-ER ROS cascades around haustoria

Considering *P. parasitica* infection induced strong mROS bursts around haustoria (Fig. 1A) and the activation of mROS triggered MAM-ROS and ER-ROS bursts (Figs. 1 and 3), we hypothesized that *P. parasitica* might also induce MAM-ROS and ER-ROS around haustoria. Both MAM-ROS and ER-ROS were activated around haustoria in *P. parasitica*–infected *N. benthamiana* leaves (Fig. 5, A and B, and fig. S11A). Together, the induced mROS, MAM-ROS, and ER-ROS around haustoria during *P. parasitica* infection (Figs. 1A and 5, A and B) suggest that the mitochondria-MAM-ER ROS cascade is likely triggered at infection sites. However, to rule out the possibility that *P. parasitica* infection individually activated ROS bursts at these three sites, we further examined potential mitochondria-MAM-ER ROS cascades at the infection sites.

We first modified mROS levels around haustoria and then analyzed MAM-ROS and ER-ROS. Increasing mROS by *NbRTP7* silencing led to enhanced MAM-ROS and ER-ROS signals around haustoria (Fig. 5C and fig. S11B), whereas mROS scavenging by MitoTEMPOL or NAC treatment reduced MAM-ROS and ER-ROS (Fig. 5, C and D, and fig. S11C), indicating that the MAM-ROS and ER-ROS bursts around haustoria are linked with mROS levels. We next blocked mROS release by inactivating mPTP via both BA treatment or *NbVDAC* silencing. Both treatments depleted ER-ROS and MAM-ROS around haustoria (Fig. 5, C and D, and fig. S11C). Additional MitoPQ treatment on *TRV-NbVDAC* leaves did not promote discernable ER-ROS and MAM-ROS bursts around haustoria, whereas ROS levels were increased in *TRV-GUS* leaves (Fig. 5, C and D, and fig. S11C), indicating the dependence of ER-ROS and MAM-ROS on mROS release around haustoria.

We next blocked the ER-ROS uptake by silencing *NbSIP1* and *NbSIP2*. This resulted in reduced ER-ROS bursts but, importantly, increased MAM-ROS around haustoria (Fig. 5, C and D, and fig. S11C). Additional MitoPQ treatment markedly increased MAM-ROS bursts but failed to enhance ER-ROS levels, suggesting mROS as the source for ER-ROS around haustoria. The inhibition of ER-lumen ROS production by *NbERO* silencing slightly reduced infection-induced ER-ROS but did not affect infection-induced MAM-ROS (Fig. 5, C and D, and fig. S11C). Notably, additional MitoPQ treatment increased MAM-ROS and ER-ROS signals in *TRV-NbERO* leaves (Fig. 5, C and D, and fig. S11C). These results indicate that the ER-ROS bursts around haustoria are partially triggered by *ERO*-produced lumenal ER-ROS, with ER-ROS being also derived from MAM.

As cpROS are induced by PTI and ETI in leaves (*14*, *35*), we investigated whether cpROS affect ER-ROS and MAM-ROS around haustoria. Blocking cpROS by the photosynthesis inhibitor 2,5-dibromo-3-methyl-6-isopropylbenzoquinone (DCMU) reduced ER-ROS signals around haustoria in a similar degree in *TRV-NbRTP7* and *TRV-GUS* leaves but had no discernable influence on MAM-ROS (fig. S11D), suggesting that cpROS partially contribute to ER-ROS in an mROS- and MAM-ROS–independent manner. We further analyzed whether RBOHs contribute to ER-ROS and MAM-ROS around haustoria. VAS2870 and GSK2795039 treatment did not affect ER-ROS and MAM-ROS around haustoria (fig. S11E), indicating that the ER-ROS and MAM-ROS were not dependent on RBOHs. Thus, our data are consistent with the conclusion that mROS initiate a mitochondria-MAM-ER ROS cascade around haustoria, independent of cpROS and apROS.

Mitochondria-ER ROS cascade and MAM formation contribute to resistance

We previously found that the *Arabidopsis rtp7* mutants showed enhanced mROS bursts and broad-spectrum resistance to different pathogens (*19*). Given our data indicating an mROS-initiated mitochondria-MAM-ER ROS cascade at the infection site, we analyzed contribution of this cascade to plant resistance.

We first tested whether blocking ROS transport from mitochondria and ER could affect plant resistance. Infection assays with *P. parasitica* zoospores on *TRV-GUS*, *TRV-NbSIP1*, and *TRV-NbSIP2* (inhibiting ER ROS transport) as well as *TRV-NbVDAC* (inhibiting mROS release) *N. benthamiana* leaves showed that silencing of *NbSIP1/2* or *NbVDAC* suppressed *N. benthamiana* resistance (Fig. 6, A and B). MitoPQ treatment increased resistance of *TRV-GUS* but not *NbSIP1/2*- and *NbVDAC*-silenced plants (Fig. 6, C and D), suggesting that the blocking of either ER import of MAM-ROS or mROS release attenuates mROS-mediated plant resistance.

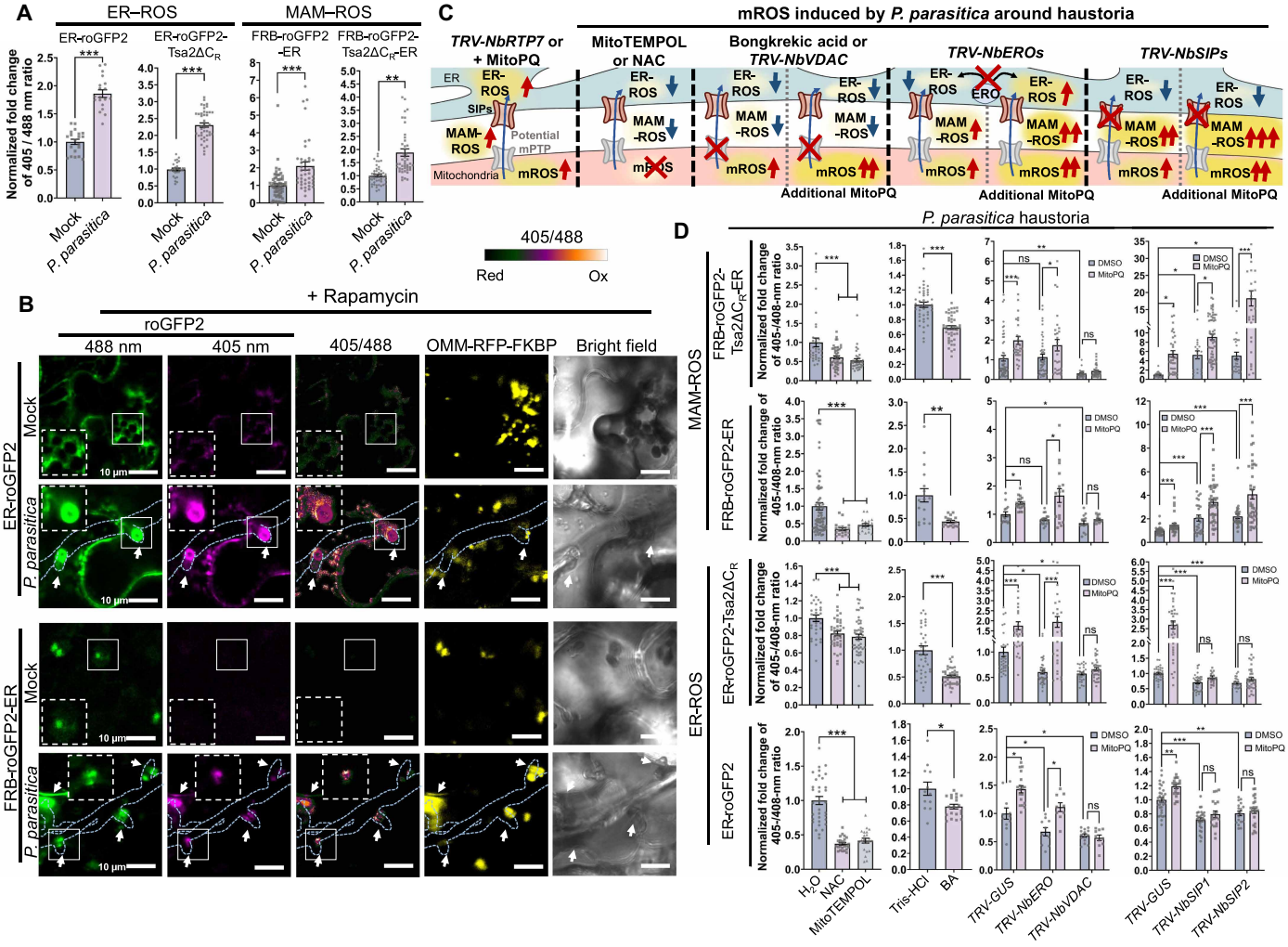

Fig. 5. mROS initiate mitochondria-ER ROS cascade around haustoria. (**A** and **B**) Confocal microscopy analysis (A) and images (B) of ROS levels in the ER lumen and MAM around *P. parasitica* haustoria in *N. benthamiana* leaves. White arrows mark *P. parasitica* haustoria. The ratio of emissions at 405/488 nm was measured by ImageJ. Rapamycin treatments were performed ~30 min before imaging. Water inoculation was the mock treatment. Scale bars, 10 μm. Data points represent different ER regions or MAMs. Dashed squares define the magnified inset images. The dashed lines mark *P. parasitica* hyphae on focal plane. (**C**) Summary of changes in ROS levels in MAM and ER lumen around *P. parasitica* haustoria in different treatments [(C); fig. S11]. Red arrows depict increasing levels, blue arrows depict decreasing levels, and red crosses depict loss or impairment of indicated transport functions. (**D**) Detection of MAM-ROS and ER-ROS levels around haustoria in *N. benthamiana* leaves using roGFP2-Tsa2ΔC$_R$ and roGFP2. *TRV-NbERO*, *TRV-NbVDAC* and *TRV-NbSIP1*, *TRV-NbSIP2* leaves were treated with MitoPQ, NAC, MitoTEMPOL, or BA and challenged with *P. parasitica*. All confocal images were taken and analyzed at ~20 hours postinoculation (hpi) with *P. parasitica* zoospores. All bars are presented as the means ± SE. Statistical significance was assessed by two-tailed Student's *t* test (A), and BA treatments in (D), one-way ANOVA with Dunn's post hoc test against water [NAC, MitoTEMPOL treatment in (D)], or two-way ANOVA with Dunn's and Bonferroni's post hoc test [for assays in *TRV-NbERO*, *TRV-NbVDAC*, and *TRV-NbSIP* leaves in (D)]. $^*P < 0.05$, $^{**}P < 0.01$, $^{***}P < 0.001$. Data points represent MAM or ER signals around different haustoria from at least four biological repeats. All the experiments were repeated three times with similar results.

We next analyzed whether ER-lumen ROS functions in immunity using inoculation assays on *TRV-NbERO* leaves. Blocking ROS production in ER-lumen by *NbERO*-silencing increased plant susceptibility to *P. parasitica* (Fig. 6A). Additional MitoPQ treatment abolished susceptibility mediated by *NbERO* silencing (Fig. 6, C and D), suggesting that ER-ROS bursts contributed to plant resistance and higher mROS levels could restore resistance impaired by attenuating ER-ROS levels. These data indicate that the mROS-initiated mitochondria-MAM-ER ROS cascade contributes to resistance.

Next, we analyzed whether MAM formation is required for immunity. Promoting MAM formation by overexpression of *ER-GFP$_{\beta 11}$* and *OMM-GFP$_{\beta 1-10}$* for an extended period (*52*) enhanced *N. benthamiana* resistance to *P. parasitica*, but this was abolished by mROS scavenging (Fig. 6E), indicating that mROS cascade is crucial for MAM formation–mediated effective immunity. These results indicate that mROS-initiated MAM formation is required for resistance.

Mitochondria-ER ROS cascade activates immune pathways associated with ER-UPR

mROS-triggered ER-ROS bursts and redox disruption in the ER lumen would affect oxidative protein folding and stimulate the unfolded protein response (UPR) (*21*, *53*). We previously showed that genetic complementation of *RTP7* or *nad7* in *rtp7-1* background

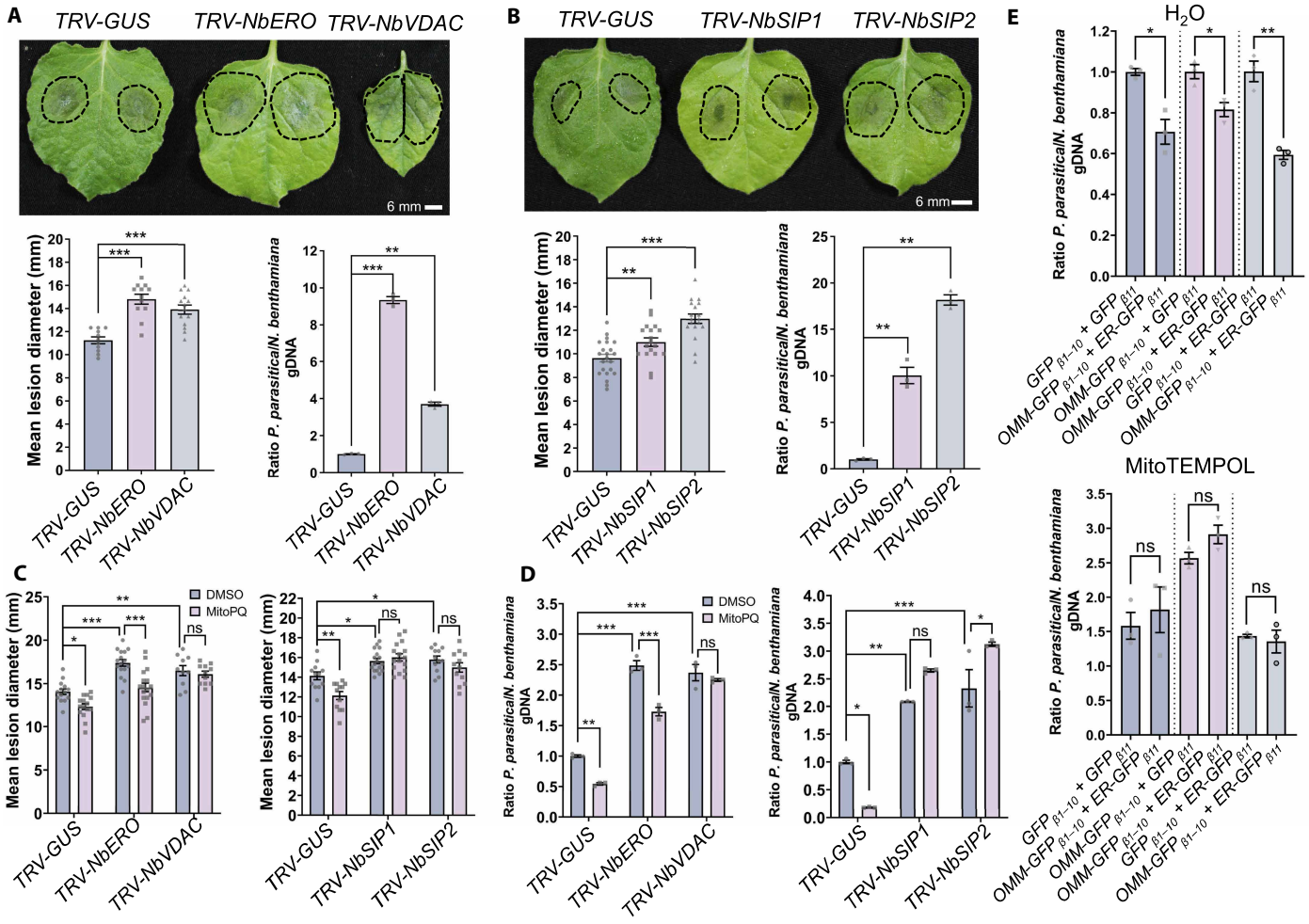

Fig. 6. mROS are required for mitochondria-ER ROS cascade- and MAM-formation- mediated plant immunity. (**A** and **B**) Silencing of *NbERO* and *NbVDAC* (A) and *NbSIP1* and *NbSIP2* (B) leads to enhanced *N. benthamiana* susceptibility to *P. parasitica*. Images of leaf phenotypes (top), mean lesion diameters, and relative pathogen gDNA contents (pathogen biomass, bottom) were taken or sampled at ~36 hpi. Scale bars, 6 mm. (**C** and **D**) Mean lesion diameter (C) and biomass of *P. parasitica* (D) in *TRV-NbERO*, *TRV-NbVDAC*, *TRV-NbSIP1*, and *TRV-NbSIP2 N. benthamiana* leaves upon MitoPQ treatment. (**E**) *P. parasitica* colonization (biomass) in *N. benthamiana* leaves coexpressing *OMM-GFP*$_{\beta 1-10}$ and *ER-GFP*$_{\beta 11}$ upon MitoTEMPOL treatment. Data points represent lesions from different leaves (for lesion diameter assays) or biological repeats (for biomass, two infected leaves were gathered together as one repeat). Bars are presented as the means ± SE. Statistical significance was assessed by one-way ANOVA with Dunn's test [(A) and (B)], two-way ANOVA with Tukey's test [(C) and (D)], or two-tailed Student *t* test (E). $*P < 0.05$, $**P < 0.01$, and $***P < 0.001$. All the experiments were repeated at least two times with similar results.

could reduce mROS in *rtp7* (*19*). We used these two complementation lines as the mROS-reducing lines of *rtp7* mutants. UPR marker genes *BiP3* (*BINDING PROTEIN 3*), *bZIP28* (*BASIC LEUCINE ZIPPER MOTIF 28*), *bZIP60* (*BASIC LEUCINE ZIPPER MOTIF 60*), *PDI* (*PROTEIN DISULFIDE ISOMERASE*), and *CNX2* (*CALNEXINS 2*) (*49*, *54*, *55*) were all statistically significantly up-regulated in *rtp7* mutants compared to Col-0, but not in the wild type in *rtp7-1* complemented with *RTP7* (*RTP7*^{comp}) or fully processed *nad7* (*nad7*^{comp}) (Fig. 7A and fig. S12A). Moreover, MitoPQ treatment of Col-0 up-regulated these UPR marker genes, but subsequent BA treatment down-regulated their expression (Fig. 7B and fig. S12, B and C). This implies that the mROS cascade activates ER stress and UPR.

Chemical agents that interfere with ER protein folding such as tunicamycin (TM; blocks N-glycosylation) and dithiothreitol (DTT; reduces protein disulfide bonds to induce thiol-based reductive stress) can stimulate ER stress (*53*). Because the mROS cascade leads to increased ER-ROS levels, mROS might participate in redox-type ER–stress activation. Therefore, we quantified *Arabidopsis* root growth upon DTT treatment. *rtp7* showed reduced root length compared with Col-0 in early growth stage as we previously reported (fig. S12D) (*19*). However, *rtp7* mutants were more tolerant to DTT, while *RTP7* overexpression lines were more sensitive to DTT. *nad7*^{comp} and *RTP7*^{comp} lines showed restored DTT sensitivity (Fig. 7, C to E), indicating the importance of mROS in DTT tolerance. However, *rtp7* mutants were more sensitive to TM than Col-0 (fig. S12E). These data suggest that the increased mROS accumulation promotes tolerance to redox ER stress and sensitivity to TM-induced ER stress.

The UPR is critical for effective plant immunity (*49*, *54*, *55*). To determine whether mROS-responsive plant immunity involves the UPR, we assayed selected UPR-related immunity marker genes, *WRKY33* (*WRKY DNA-BINDING PROTEIN 33*) (*56*), *EFR* (*EF-TU*

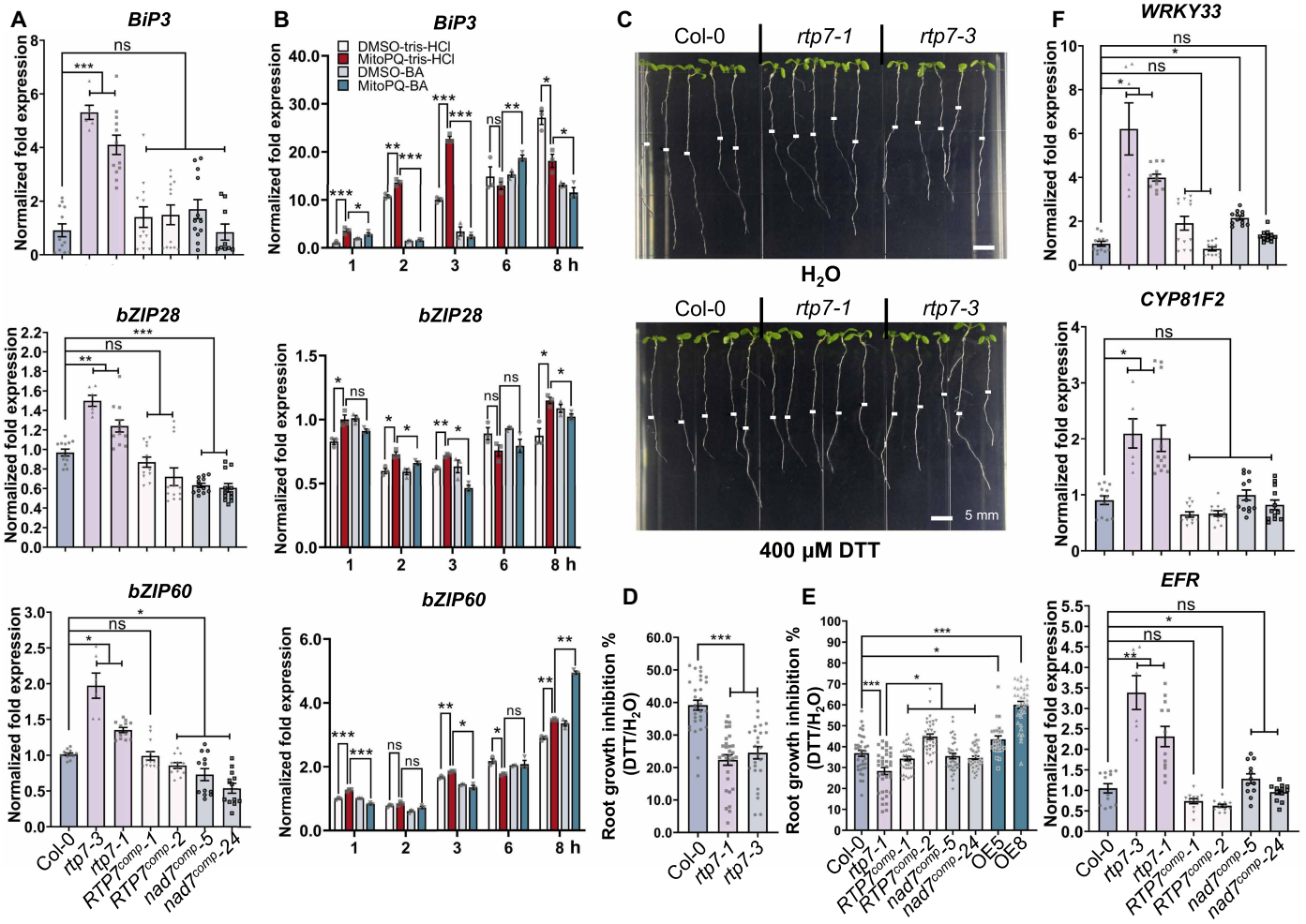

Fig. 7. Mitochondria-ER ROS induce redox ER stress and elicit ER-stress–related immune responses. (**A**) RT-qPCR assay of UPR marker genes *BiP3*, *bZIP28*, and *bZIP60* in leaves of 4-week-old *Arabidopsis* wild-type Col-0, *rtp7-1*, and *rtp7-3* mutants; *RTP7* complementation lines *RTP7*^{comp}*-1* and *RTP7*^{comp}*-2*; and *nad7* complementation lines *nad7*^{comp}*-5* and *nad7*^{comp}*-24*. Data points represent biological repeats from three independent experiments (~2 leaves from different plants gathered together as one replicate). (**B**) RT-qPCR assay of *BiP3*, *bZIP28*, and *bZIP60* in 10-day-old Col-0 seedings upon treatment with MitoPQ and BA and sampling at the indicated time points. Data points represent biological repeats (~15 seedlings gathered together as one replicate). (**C** and **D**) Comparison of *Arabidopsis* root phenotypes (C) and root growth inhibition (D) for wild-type Col-0 and *rtp7* mutants treated with DTT. White lines mark the root length when the seedlings were transferred onto plates containing DTT or control media. Scale bars, 5 mm (C). Data points represent inhibition rates of different seedlings (D). (**E**) Root growth inhibition of DTT-treated *RTP7*-related *Arabidopsis* lines. *RTP7* overexpression lines (OE5 and OE8). Data points represent inhibition rates of different seedlings. (**F**) RT-qPCR assay of UPR-related immune genes *WRKY33*, *EFR*, and *CYP81F2* in 4-week-old *RTP7*-related *Arabidopsis* lines. Data points represent biological repeats (~2 leaves from different plants gathered together as one replicate) from three independent experiments. All the bars are the means ± SE. Statistical significances were assessed by Brown-Forsythe ANOVA with Dunnett's T3 test [(A) and (F)], ANOVA with Tukey's post hoc test (E), or Dunn's test [(B) and (D)]. **P* < 0.05, ***P* < 0.01, and ****P* < 0.001. All the experiments were repeated at least two times with similar results.

RECEPTOR) (*57*, *58*), *CYP81F2* (*CYTOCHROME P450*, *FAMILY 81*, *SUBFAMILY F*, *POLYPEPTIDE 2*) (*59*), and γ*VPE* (γ *VACUOLAR PROCESSING ENZYME*) (*54*) in the wild-type Col-0, *rtp7*, *RTP7*^{comp}, and *nad7*^{comp} lines. Quantitative real-time polymerase chain reaction (qRT-PCR) analyses showed that *RTP7* negatively regulates their expression through *nad7* (Fig. 7F and fig. S12A). As *RTP7* regulates mROS through *nad7*, this result indicates that UPR-related immune genes are responsive to mROS. Furthermore, these marker genes were up-regulated in leaves of *rtp7-1* compared to Col-0 during *P. parasitica* infection (fig. S12F). Together, these results indicate that the increased mROS activate UPR pathways to coordinate enhanced plant immunity.

DISCUSSION

Here, we report a previously unknown intracellular ROS cascade, whereby mROS signals are transferred into the ER lumen to activate redox-induced and ER-stress–associated immune responses. Mitochondria and ER interorganelle contacts are required for mROS signal transfer and are stimulated by *P. parasitica*–induced mROS bursts (Fig. 8). We previously showed that mitochondrial RNA processing factor *RTP7* functions in RNA splicing of complex I transcript *NAD7*, *RTP7* knockout induced mROS bursts from complex I, and pathogen infection and flg22 treatment both down-regulate complex I–related genes such as *AtRTP7* (*19*, *60*), which supports the finding that plants generate mROS upon pathogen attack, which through MAM

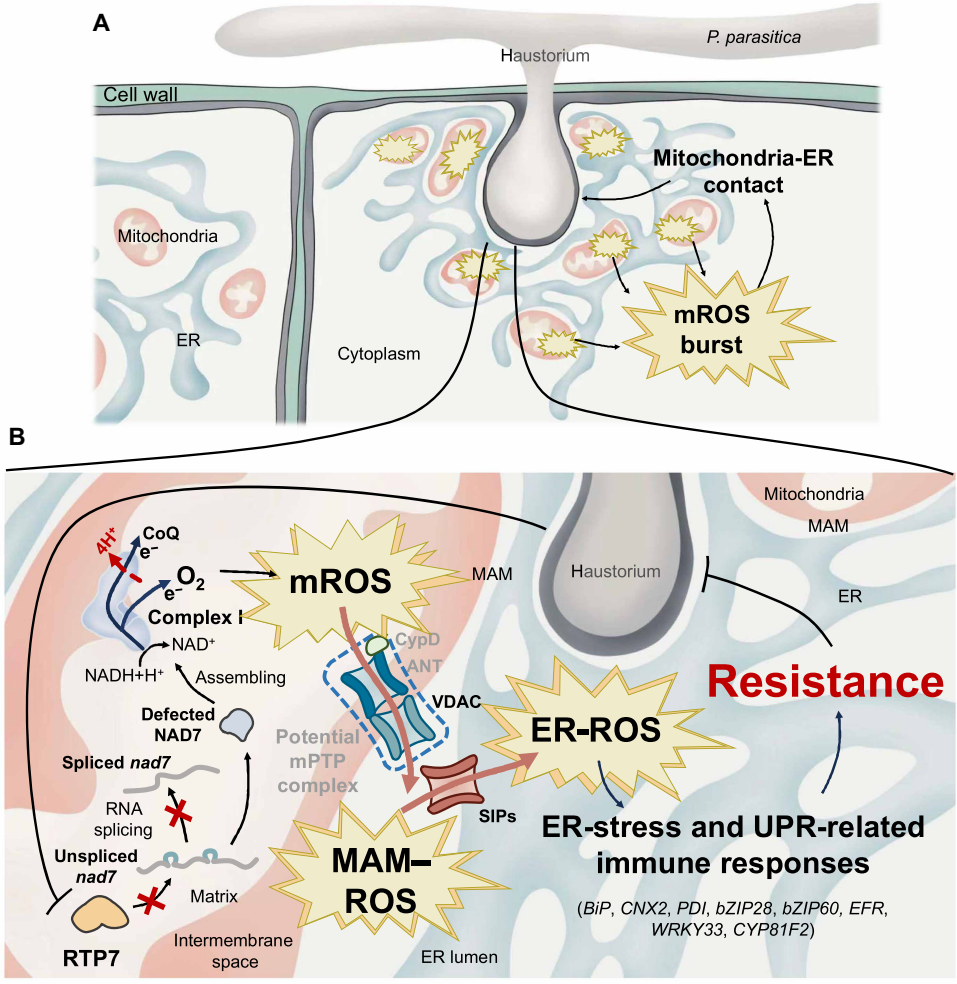

Fig. 8. Proposed model for mROS in activating plant immunity through interorganelle dialog and a mitochondria-ER lumen ROS cascade independent of apROS and cpROS. (**A**) *P. parasitica* infection induces mROS that subsequently initiate plant immune responses, including PTI, aggregation, and interaction of mitochondria and ER around haustoria. The mROS bursts further promote association of mitochondria and ER. (**B**) Infection-induced mROS, resulted from down-regulated host *RTP7* expression and reduced splicing of *NAD7*, are Complex I–related mROS bursts. The increased mROS mediate subsequent initiation of a mitochondria-ER lumen ROS cascade, leading to increased ER-ROS levels, induction of ER-stress–related immune responses, and enhanced disease resistance.

formation activates a mitochondria-ER ROS cascade, and last triggers the UPR and other ER mechanisms that activate immunity (Fig. 8).

apROS bursts and cytosolic oxidation during PTI have been shown to occur in a biphasic manner at 1 and 6 hours after MAMP treatments, and both apROS waves preceded the two cytosolic oxidation waves (*61*), suggesting that apoplastic preceded cytosolic ROS signaling. The two waves of apROS depend on RBOHD, while the two waves of cytosolic ROS are not related to RBOHD (*61*), suggesting that the cytosolic ROS do not originate from apoplast. As chloroplast, mitochondria, ER, and peroxisomes are sources for cytosolic ROS in plant cells (*5*), and we showed that mROS bursts are not related to RBOHs (Fig. 4H and figs. S9 and S11), our data support the conclusion that the observed cytosolic ROS was independent from apROS. Moreover, cytosolic ROS waves depend on the membrane coreceptor, BAK1 (BRI1-ASSOCIATED RECEPTOR KINASE 1) (*61*), demonstrating that the membrane signaling precedes, and is crucial for cytosolic ROS bursts. How the membrane signaling reaches and triggers cytosolic ROS remains to be determined.

Mitochondrial respiration and ER stress were reported to be linked in plants, and ROS might be the key signaling factor between these two organelles (*21*, *62*). Mitochondrial complex I and complex III are two major production sites of mROS (*27*). The inhibition of complex III by antimycin A induced the expression of *ALTERNATIVE OXIDASE 1A* (*AOX1a*) to relieve the mitochondrial dysfunction caused by blocking of electron transport and mROS production (*63*). The transcriptional activation of *AOX1a* upon antimycin A treatment was mediated by two ER membrane–localized transcription factors, NAC013 and NAC017 (*21*), indicating that ER is involved in the regulation of mitochondrial function. Moreover, *AOX1a* silencing reduced plant tolerance to DTT-induced ER stress (*21*), further indicating that the mitochondria and ER are functionally linked. The mitochondrial complex I inhibitor rotenone induces mROS bursts and expression of multiple UPR genes in *Arabidopsis* (*62*). We showed that the increase of complex I–related mROS levels by *AtRTP7* knockout or MitoPQ treatment also induced UPR in the ER, further reinforcing the link between mitochondrial respiration and ER. These

results suggest that mROS from complex I or complex III both could be involved in mitochondria-ER cross-talk.

The ER is the central organelle for the production and secretion of immune proteins, and its efficacy depends on coordinated activation of the UPR (*49*, *55*, *64*). We found that increased mROS induced the expression of several ER-stress–related immune genes during *P. parasitica* infection, suggesting that mROS initiate the UPR to enhance the efficacy of immune responses (Fig. 7 and fig. S12). Distinct UPR pathways are activated by different ER stress sensors. In addition to ER-membrane–associated transcription factors bZIP17 and bZIP28, the protein kinase IRE1 (which targets bZIP60) serves as an ER stress sensor to launch the UPR (*53*). Both *bZIP28* and *bZIP60* are up-regulated in *rtp7* (Fig. 7), suggesting a function of mROS in activating these pathways. However, *rtp7* showed different responses to DTT- and TM-induced ER stress (Fig. 7 and fig. S12), suggesting that mROS might function differently in these pathways. As mROS promote ER-mitochondria contacts, it will be informative to further examine their role in UPR activation and investigate mechanisms of mROS activation in these distinct pathways. However, as mitochondria are a signal hub in immunity (*65*), it is important to determine whether *rtp7*-mediated resistance is fully dependent on ER-related immune responses.

The mROS release is mediated by the mPTP, which contains two inner mitochondria membrane–localized components, ANTs and CypD, and outer mitochondria membrane–localized VDAC proteins (*29*). Although the mPTP formation and function in plants remain unclear, there is increasing evidence suggesting that plants might have similar mPTPs, as animals (*66*). mPTP formation and opening induce decreased mitochondrial membrane potential ($\Delta\Psi m$) and mitochondrial swelling (*30*). Therefore, their measurements are widely used methods to detect mPTP functions (*30*). We found that *P. parasitica* infection or flg22 treatment reduced $\Delta\Psi m$ (fig. S1) and that mitochondria gathered around *P. parasitica* haustoria are bigger in size than that of uninfected cells (fig. S1). These results indicate a potential role of mPTP formation and opening in plant immunity, although we have not directly identified specific mPTP subunits. It would be worth further to investigate plant mPTP subunits and its formation in detail during pathogen infection.

VDACs are components of the mPTP complex that localizes at the OMM, functioning as channels that mediate material transport, and may also function as physical linkers in MAM formation (*29*, *45*). VDACs interact with the cytosolic chaperone glucose-regulated protein 75 (GRP75) and the ER-resident Ca^{2+} channel inositol 1,4,5-trisphosphate receptor (IP_3R) to form the IP_3R-GRP75-VDAC complex that functions in both Ca^{2+} translocation from the ER into mitochondria and the physical MAM linkers (*45*).We found that mROS-induced mitochondria-ER interaction was significantly reduced in the *NbVDAC*-silenced leaves, while BA treatment showed no discernable effects (fig. S7), indicating that mROS release per se might not be crucial for mROS-promoted mitochondria-ER interaction. Instead, mROS produced in the mitochondrial matrix might promote the mitochondria-ER interaction through an unknown mechanism. However, considering that BA inhibits the opening of adenine-nucleotide translocators on the inner mitochondria membrane (*29*, *31*), mROS transfer across the inner membrane is apparently not required.

We showed that mROS induction in plant cells promoted MAM formation (Fig. 2). Together, a recent report on mROS-induced MAM formation in HeLa cells (*67*), mROS-mediated MAM formation might be conserved in animals and plants. Moreover, two tethering factors, RMDN3 (regulator of microtubule dynamics protein 3) and VAPB (vesicle-associated membrane protein-associated protein B) (*67*), that mediate mROS-induced MAM formation were identified in mammalian cells. Therefore, we further analyzed whether these two tethering factors might function in plant mROS-induced MAM formation. However, while we found VAPB homologs in the *Arabidopsis* genome, we were unable to find RMDN3 homologs, suggesting that although mROS-induced MAM formation is detected in both plants and mammalian cells, the involving factors are most likely not fully conserved. Because little is known on organellar tethering factors in plants, targeted mutations and chemical-inhibitor screens would be necessary to identify interacting proteins of VAPB, VDAC, and SIPs to provide mechanistic insights into the formation of mitochondria-ER contacts during plant immunity.

Organelle interactions are involved in lipid and ion transfer, signaling, and organelle division in animals and yeasts (*22*), but these functions in plant immunity remain unclear. Current ROS staining methods do not provide necessary resolution to quantify MAM-ROS at the ER-mitochondrial interface. Our chemically inducible synthetic linker adapted mammalian systems and genetically encoded split-GFP assays, allowed unveil of a mitochondria-ER ROS cascade and mROS-induced MAM formation. These methods can be deployed in parallel in transient assays, providing an efficient experimental approach to reveal interactions and roles of other organelles in plant immunity.

Limitation of this study

We showed an intracellular ROS cascade whereby mROS signals are transferred into ER lumen to trigger UPRs and enhanced plant immunity, independent of apROS and cpROS. We adapted chemically inducible synthetic linkers to target ROS sensors and quantify MAM-ROS levels. We further used split-GFP assays to study and define mitochondria-ER contact sites. We noticed that extended overexpression (>3 days) of fusion proteins (e.g., FRB-roGFP2-ER or ER-$GFP_{\beta 11}$) to the ER surface could elicit plant cell death, and extended transient expression in *N. benthamiana* could lead to irreversible accumulation of GFP signals in the split-GFP assays. These issues can be solved by optimizing experimental conditions for transient expression of these GFP biosensors. However, the overexpression of *FRB-roGFP2-ER* or *ER-GFP$_{\beta 11}$* resulted cell death; thus it is not possible to obtain transgenic *Arabidopsis* lines for their stable expression, limiting the employment of these two ROS and MAM detection methods in different species. Another limitation of the study is that the mitochondria-ER ROS cascade mediated activation of resistance to other pathogens requires additional verification, as *rtp7* mutants were previously shown to be resistant to broad-spectrum pathogens.

MATERIALS AND METHODS

Plant-growth conditions and *Arabidopsis* transformation

The *Arabidopsis* T-DNA insertion lines *rtp7-1* (SALK_085606C) (*19*), *rtp7–3* (SALK_029012C) (*19*), *rbohD* (SALK_109396C) (*19*), *vdac3* (SALK_127899C), *ero1-1* (SALK_020128C), *ero1-2* (SALK_050000C), *ero2* (SALK_201119C), *sip1;1-1* (SALK_069427C), and *sip1;1-2* (SALK_052779C) were obtained from the Arabidopsis Biological Resource Center (ABRC). Homozygous lines were confirmed by PCR, and primers used are listed in table S1. The gene expression

levels of *vdac3*, *ero1-1*, *ero1-2*, *ero2*, *sip1;1-1*, and *sip1;1-2* mutants were confirmed (fig. S13).

All transgenic *Arabidopsis thaliana* lines were generated using the floral-dip method and screened on half-strength Murashige and Skoog (1/2 MS) plates with the appropriate antibiotics (*68*). The complementation lines: $RTP7^{comp}$, $nad7^{comp}$ in *rtp7* background, and *RTP7* overexpression lines in Col-0 background were previously reported (*19*).

For *Arabidopsis* root assays, seeds were surface sterilized with 75% ethanol and 1% NaClO and sown on 1/2 MS plates. Plants were grown in a growth chamber (Ningbo Dongnan Instrument Co. Ltd., GDN) at 23°C with ~120 μmol photons m^{-2} s^{-1}, 16-hour light/8-hour dark, following 2 days of stratification at 4°C.

For transient expression or pathogen inoculation on leaves, *Arabidopsis* and *N. benthamiana* seeds were grown in a mixture of vermiculite and nutritive soil (1:2) under the following conditions: ~120 μmol photons m^{-2} s^{-1} with light-emitting diode lamps (OUTRACE, OU016-U4B) and 13-hour light/11-hour dark at 23°C with 60 to 70% relative humidity.

Plasmid constructs

The sequences encoding the human *FKBP* domain (*69*), *FRB* domain (*70*), $GFP_{\beta 1-10}$ and $GFP_{\beta 11}$ (*71*), ER surface-tether sequence (C-terminal 521 to 587 segment of the phosphoinositide phosphatase Sac I: NCBI reference sequence: NM_001319073.2), OMM-tether sequence (TOM70 protein channel, Gene ID: 855602) (*72*), *roGFP2* (*73*), roGFP2-Tsa2ΔC$_R$ (*74*), and Grx1-roGFP2iL (*75*) were codon-optimized for *Arabidopsis* and synthesized by Beijing Tsingke Biotech Co. Ltd.

For the plant-expression construct *OMM-RFP-FKBP*, the OMM tether sequence of *TOM70* was fused to the N terminus of *RFP*, while the FKBP domain was fused to the C terminus of *RFP* using overlapping PCR and cloned into the Xba I and Xho I sites of pKannibal vector. These constructs were digested by Not I, and the resulting fragment containing *OMM-RFP-FKBP* was inserted into pART27. For the constructs *ER-roGFP2-FRB*, *ER-roGFP2-Tsa2ΔC$_R$-FRB*, and *ER-GFP-FRB*, the *GFP*, *roGFP2*, or *roGFP2-Tsa2ΔC$_R$* was fused between the *FRB* domain and the ER surface-tether sequence by overlapping PCR and cloned into pKannibal-pART27. The constructs *OMM-*$GFP_{\beta 1-10}$ and *ER-*$GFP_{\beta 11}$ were constructed similarly to *OMM-RFP-FKBP* and *ER-roGFP2-FRB* vectors with the same localization signals. To target roGFP2, roGFP2-Tsa2ΔC$_R$, and Grx1-roGFP2iL into the ER lumen, the signal sequence of *AtWAK2* (At1g21270) was fused to the N terminus of these sensors—with the ER retention signal (HDEL) fused to the C terminus of *roGFP2*, *roGFP2-Tsa2ΔC$_R$*, or *Grx1-roGFP2iL*—and cloned into pKannibal-pART27.

For VIGS of *NbVDAC* in *N. benthamiana*, the four *NbVDAC* homologs, *NbVDAC1* to *NbVDAC4* (of which *NbVDAC1* to *NbVDAC3* have high similarity), were cosilenced with two tandem fragments: one fragment for *NbVDAC1* to *NbVDAC3* silencing and one specific for *NbVDAC4* silencing. For VIGS of *NbERO*, the four *NbEROs* were cosilenced with two tandem fragments. There are four *NbSIP1* homologs and two *NbSIP2* homologs encoded in the *N. benthamiana* genome. All four *NbSIP1s* were cosilenced with two tandem fragments, one targeting *NbSIP1a* and *NbSIP1b* and the other *NbSIP1c* and *NbSIP1d*. All the silencing fragments were specific for their targets and ~300 base pairs in length. These fragments were amplified from *N. benthamiana* cDNA and digested by Eco RI and Xho I and inserted into pTRV2.

Other plasmid constructs were as previously described (*19*, *76*). All primers are listed in table S1.

VIGS in *N. benthamiana*

VIGS in *N. benthamiana* was performed as previously described (*19*, *76*, *77*). *Agrobacterium tumefaciens* GV3101 containing *pTRV1*, *pTRV2-NbVDAC*, *pTRV2-NbERO*, *pTRV2-NbSIP1*, *pTRV2-NbSIP2*, *pTRV2-NbRTP7*, *pTRV2-GUS*, or *pTRV2-PDS* was grown for 36 hours at 28°C in LB medium with appropriate antibiotics. Bacteria were collected and resuspended in infiltration buffer (10 mM MES, 10 mM $MgCl_2$, and 200 mM acetosyringone, pH 5.6). Bacteria harboring *pTRV1* and those harboring *pTRV2* target genes were mixed in a 1:1 ratio, and the final optical density at 600 nm (OD_{600nm}) for each strain was adjusted to 0.25. The cocultures were infiltrated into 4-week-old *N. benthamiana* leaves and grown for ~14 days before being used for pathogen inoculation and ROS detection assays. Silencing of target genes was confirmed (fig. S13).

Pharmacological challenge of *N. benthamiana* and *Arabidopsis*

The stock solutions of MitoPQ (MitoParaquat, MedChem Express, HY-130278), TM (Shanghai Yuanye Bio-Technology, S17119), DCMU (MedChem Express, HY-B0860), DPI (Sigma-Aldrich, D2926), VAS2870 (MedChem Express, HY-12804), GSK2795039 (MedChem Express, HY-18950), and rapamycin (MedChem Express, HY-10219) were prepared in DMSO. DTT (Shanghai Yuanye Bio-Technology, S11080), MitoTEMPOL (MKbio, MX4808), and NAC (MKbio, MS0458) were dissolved in ddH_2O. BA (Sigma-Aldrich, B6179) was dissolved in 10 mM tris-HCl (pH 7.5). Unless otherwise specified, the chemicals used for experimentation were diluted to their final concentration with ddH_2O as follows: 0.5 μM MitoPQ, TM (50 ng/ml), 1 μM rapamycin, 10 μM DCMU, 10 μM DPI, 400 μM DTT, 10 μM MitoTEMPOL, NAC (10 μg/ml), 10 μM BA, 50 μM VAS2870, and 25 μM GSK2795039.

For treatments upon *P. parasitica* inoculation, leaves were gathered and the appropriate chemical applied to cotton strips that were wrapped around leaf petioles to avoid the direct effect of the chemical on the pathogen. An equal volume of the final concentration of the specific chemical solvent diluted in ddH_2O were used as controls. Leaves were inoculated with *P. parasitica* zoospores ~1 hour after chemical treatment.

For mROS staining by chemical treatment, MitoPQ or BA was added into the staining solution and incubated for 1 to 2 hours. TM and DTT treatments on *Arabidopsis* seedlings were conducted as previously described (*42*, *49*). For DTT treatment, plants were grown for 5 days on control MS media before transfer to 400 μM DTT. Root elongation was scored 5 days after DTT treatment. For TM treatment, 4-day-old seedlings were transferred in liquid medium with TM (50 ng/ml) or 0.01% DMSO (v/v). Seedling fresh weight was determined at 7 days posttreatment.

roGFP2-based ROS sensors for ER-ROS detection

The H_2O_2 sensor roGFP2-Tsa2ΔC$_R$ was reported to be nearly fully oxidized in the ER lumen in normal plant cells, and it is thus impossible to further probe higher ER-ROS levels using plate readers (*78*). In our hands, different growth stages and propagation conditions affected oxidation rates of ER-roGFP2-Tsa2ΔC$_R$. As we aimed to detect ER-ROS under pathogen inoculation, the leaves need to be cocultured with the pathogen in darkness for at least 16 hours to promote

infection. Therefore, we first detected the oxidation rate of ER-roGFP2-Tsa2ΔCR in ~4-week-old *N. benthamiana* leaves under ~16-hour dark treatment. This showed reduced oxidation rate compared to the leaves kept under normal growth conditions with light (from 95 to 81%; fig. S2C). We also confirmed the oxidation rate of ER-roGFP2 to be ~80% when cultured in the dark for ~16 hours in ~4-week-old *N. benthamiana* leaves (fig. S2C), which is very similar to the oxidation rate of ER-roGFP2-Tsa2ΔC$_R$ under similar growth conditions. Furthermore, when transiently expressed in older *N. benthamiana* leaves (~6 weeks old) that we used for most of our imaging assays, ER-roGFP2-Tsa2ΔCR showed ~70% of full oxidation under dark treatment (fig. S2, D and E). These results indicate that with dark treatment, roGFP2 and ER-roGFP2-Tsa2ΔC$_R$ could be used for ER-ROS detection. The oxidation rates of roGFP2 sensors were calculated as reported (*78*).

Grx1-roGFP2iL was reported to have a reduced oxidation rate compared with roGFP2; therefore, it is more suitable for ER redox detection (*42*). We first detected the MitoPQ-induced ER-ROS burst in *N. benthamiana* leaves using ER-targeted biosensors Grx1-roGFP2iL (ER-Grx1-roGFP2iL), ER-roGFP2, and ER-roGFP2–Tsa2ΔC$_R$. MitoPQ-induced ER-ROS could be detected by all three sensors (fig. S2F). Consistent with previous reports (*42*), ER-Grx1-roGFP2iL provided stronger fold change than the other two sensors upon MitoPQ treatment (36% increase compared with a 21 to 29% increase). These results indicate that both roGFP2 and roGFP2-Tsa2ΔCR could be used for ER-ROS detection, although with smaller fold changes. In this study, all ER-ROS detection was done using these three sensors: ER-Grx1-roGFP2iL, ER-roGFP2, and ER-roGFP2-Tsa2ΔC$_R$ with consistent results.

MitoPQ treatments

We tested MitoPQ concentrations (10 nM, 50 nM, 100 nM, 0.5 μM, 5 μM, and 10 μM) on ~8-day-old *Arabidopsis* roots. mROS were stained with MitoTracker Red, and CM-H$_2$DCFDA and fluorescent signals were observed under a confocal microscope 2 to 3 hours posttreatment. To compare ROS levels for different MitoPQ concentrations, all parameters and confocal settings were kept the same.

MitoPQ (50 nM) was sufficient for mROS elicitation, although fewer cells showed detectable mROS signals (fig. S4A). MitoPQ treatment (100 nM) triggered a stronger mROS response than 50 nM, and 0.5 μM MitoPQ triggered the strongest mROS signals without notable changes in morphology. However, we found that 5 μM MitoPQ treatment resulted in cell damage, as evidenced by cell shrinkage. As a consequence, DCF signals were only observable in the deeper cortical cells. MitoPQ (10 μM) treatment showed similar cellular changes as 5 μM MitoPQ, and notably, both MitoTracker Red and DCF signals were reduced or absent from these shrunken cells (fig. S4, A and B). Therefore, we chose 0.5 μM as the (noncytotoxic) concentration to use with *Arabidopsis* roots.

Next, we detected mROS levels in *Arabidopsis* roots at different time points (1, 2, 3, 6, and 8 hours) post–0.5-μM MitoPQ treatment. With 1-hour treatment, an mROS burst was detected, with a trend to increase in strength until 6 hours. However, at both 6 and 8 hours, there were no longer detectable differences in mROS levels (fig. S12B). In turn, ER-ROS could be detected at 1 hour and became steadily stronger until 6 hours. Together, our experimental approach was to determine mROS levels post–0.5-μM MitoPQ treatment for ~2 hours, unless otherwise specified.

For MitoPQ treatment in *N. benthamiana* leaves, we routinely use leaves of ~6-week-old *N. benthamiana* plants for pathogen inoculation and ROS detection. We used mitochondrial matrix–targeted roGFP2-Tsa2ΔC$_R$ (mt-roGFP2-Tsa2ΔC$_R$) to detect mROS. We performed MitoPQ treatment with two different methods: (i) MitoPQ solution was used to immerse leaves for ~3 hours, and (ii) MitoPQ solution was applied to cotton strips that were used to wrap around leaf petioles and cultured in the dark for at least 16 hours. Method 1 was routinely used for MitoPQ treatment with no *P. parasitica* inoculation. Method 2 was used for MitoPQ treatment upon *P. parasitica* inoculation. For pathogen infection, we needed to coculture leaves with pathogen in the dark for at least 16 hours. To avoid direct effect of MitoPQ on the pathogen, MitoPQ was added in the cotton strips. Different MitoPQ concentrations (0.5, 5, 25, and 50 μM) were tested for both methods, with the same volume of DMSO as mock control.

Using method 1, all MitoPQ concentrations triggered mROS bursts (fig. S4C). With the increase of MitoPQ concentration, mROS levels also increased. Treatments with 0.5 and 5 μM MitoPQ did not affect mitochondrial morphology in *N. benthamiana* leaves, while treatments with 25 and 50 μM MitoPQ changed mitochondrial morphology (fig. S4C).

Using method 2, MitoPQ concentrations of 0.5, 5, and 25 μM showed activated mROS bursts (fig. S4C). A 25 μM MitoPQ treatment induced weaker mROS than that of 0.5 and 5 μM MitoPQ treatment, and the highest concentration (50 μM) of MitoPQ did not trigger mROS (fig. S4C). The high MitoPQ concentration might have induced cell death in the leaf petioles, which inhibited MitoPQ absorption. All tested MitoPQ concentrations did not affect mitochondrial morphology in *N. benthamiana* leaves.

We found that compared with *Arabidopsis* roots, *N. benthamiana* leaves showed stronger tolerance to MitoPQ, as 5 μM MitoPQ was cytotoxic to *Arabidopsis* roots, but not to *N. benthamiana* leaves. Together, as 0.5 μM MitoPQ could trigger mROS burst, we used 0.5 μM MitoPQ in both method 1 and method 2 for MitoPQ treatments in *N. benthamiana* assays.

Split-GFP–based MAM formation detection in plant cells

GFP was separated into two parts to receive nonfluorescing GFP$_{\beta 11}$ and GFP$_{\beta 1-10}$ fragments. We fused the ER-membrane–anchoring sequence with GFP$_{\beta 11}$ (ER-GFP$_{\beta 11}$) to tether it to the cytoplasmic surface of ER membranes. GFP$_{\beta 1-10}$ was then linked to the OMM-anchoring sequence (OMM-GFP$_{\beta 1-10}$) to tether it to the cytoplasmic surface of the OMM. Transient coexpression of different combinations of *GFP$_{\beta 11}$*, *GFP$_{\beta 1-10}$*, *ER-GFP$_{\beta 11}$*, and *OMM-GFP$_{\beta 1-10}$* in *N. benthamiana* leaves, with ER-CFP and mt-RFP markers, indicated that only *ER-GFP$_{\beta 11}$* and *OMM-GFP$_{\beta 1-10}$* could confer strong GFP fluorescence between mitochondria and ER (fig. S6, A and B), thus demonstrating specificity of the assay in plant cells.

Using more sensitive confocal settings, cytoplasmic localization could be observed when transient expressed *GFP$_{\beta 11}$* + *GFP$_{\beta 1-10}$* (fig. S6C). The ER network was observed in ER-*GFP$_{\beta 11}$* + *GFP$_{\beta 1-10}$* group (fig. S6C). Mitochondria-like small dots could be observed in *GFP$_{\beta 11}$* + OMM-*GFP$_{\beta 1-10}$* group (fig. S6C). These results are consistent with previous reports (*79*). However, using these settings, the *ER-GFP$_{\beta 11}$* + *OMM-GFP$_{\beta 1-11}$* signals were highly oversaturated in which the small dot-like signals even appearing to coalesce (fig. S6, C and D). As our objectives were to determine and visualize MAM

formation, we applied settings suitable for detection of *ER-GFP*$_{\beta 11}$ + *OMM-GFP*$_{\beta 1-11}$.

We quantified mitochondria-ER contacts using three parameters: total fluorescence intensity per cell, the percentage of cell area occupied by GFP fluorescence, and the total number of fluorescent foci (spots) per cell (*43*). *ER-GFP*$_{\beta 11}$ and *OMM-GFP*$_{\beta 1-10}$ expression was similar in one experiment site (fig. S10).

Overtargeting ER-GFP$_{\beta 11}$ to the ER surface causes plant cell death, and extended (>3 days) transient expression in *N. benthamiana* could lead to irreversible accumulation of GFP signals in split-GFP assays. However, these issues can be solved by optimizing experimental conditions (2 days of expression at OD_{600nm} = 0.2) for transient expression.

Live-cell imaging

For mROS staining, *Arabidopsis* roots or *N. benthamiana* leaves were stained with 200 nM MitoTracker Red CMXRos (Invitrogen, M7512) to mark mitochondria and 10 μM CM-H_2DCFDA (2′,7′-dichlorodihydrofluorescein diacetate, MKbio, MX4827) to stain ROS for 1 to 2 hours. These samples were washed with ddH_2O twice before imaging.

To detect MAM-ROS signals, *N. benthamiana* leaves were coinfiltrated with *A. tumefaciens* GV3101 cells carrying *FRB-roGFP2-ER* and *OMM-RFP-FKBP* constructs, respectively, and propagated for 2 days. For MitoPQ, BA, or other chemical treatments without *P. parasitica* inoculation, solutions were infiltrated into *N. benthamiana* leaves ~3 hours before observation. For chemical treatments that aimed to analyze their influence on the ROS levels around *P. parasitica* haustoria, *FRB-roGFP2-ER*– and *OMM-RFP-FKBP*–expressed leaves were harvested and inoculated with *P. parasitica* zoospores at 1 days postinfiltration (dpi), and the solutions were added onto the cotton strips wrapped around the petioles. The inoculated leaves were further propagated for 16 to 24 hours before observation. Inoculated leaf sections were cut into small pieces and immersed in inducing solution containing 1 μM rapamycin for ~30 min before imaging. The detection of ER-ROS using ER-lumen-roGFP2 sensors were conducted similarly to the detection of MAM-ROS.

For split-GFP assays, *N. benthamiana* leaves were infiltrated with *OMM-GFP*$_{\beta 1-10}$ and *ER-GFP*$_{\beta 11}$ for 2 days. Confocal images displayed as the maximum projection of the *z* axis were used for analysis.

Confocal imaging was carried out using a Leica TCS SP8 microscope or an Olympus FV3000 microscope. CFP was imaged using an excitation wavelength of 405 nm with emission collected at 420 to 480 nm. DCF or GFP was excited at 488 nm with emissions collected at 500 to 540 nm. MitoTracker Red CMXRos and RFP were imaged using an excitation wavelength of 552 nm with emission collected at 580 to 630 nm. roGFP2 was excited at 405 and 488 nm, and the respective emissions were collected at 510 to 550 nm. All the parameters and settings of confocal microscopes were kept the same for the samples in an experiment to ensure images from different samples were comparable.

To avoid selection bias, which is a technical challenge in microscopy observations (*80*), we used several observation and analyses protocols. For the mROS detection in *Arabidopsis* roots, the imaging fields (we normally chose the elongation area) were selected by eyepiece observation in bright field. The fluorescence of the samples was not observed in eyepiece to avoid the photobleaching or any selection on the fluorescence-dependent imaging fields. Then, the observation mode was directly switched to the confocal observation, and the images were taken, with no movement of the imaging field. Once the samples were observed, the images must be taken and analyzed. For the detection of ROS sensors without pathogen inoculation, the image process was similar to the observation of *Arabidopsis* roots.

For the ROS sensor detection around *Phytophthora* haustoria, the image fields were selected by eyepiece observation in bright field, with the leaf area at the junction of diseased and healthy tissue was chosen. As the haustoria were not very easy to be found, when the pathogen was not labeled by fluorescence protein and the haustoria did not always invade the sensor-expressed leaf cells, the bright field (used for locating haustoria) and fluorescence channel elicited by 488-nm laser (used to find the senser-expressed cells) were used for real-time observation under confocal imaging mode. Because roGFP2 redox status is represented by the ratio of 405-nm elicited fluorescence to 488-nm elicited fluorescence, choosing cells based on observation of only one channel (488 nm) would avoid selection bias but guarantee the sensor expression. Then, the images of haustoria that invaded sensor expression cells were taken. All the identified haustoria were imaged and analyzed.

The captured images were analyzed by ImageJ. To avoid biased selection of the cells or mitochondria, the mitochondria used for mROS measurements were selected in the MitoTracker red channel where the ROS levels are not shown. Then, the mean gray value of the selected mitochondria was directly measured in DCF channel. For the analyses of the ratio of the ROS sensors, the examined areas were also chosen in one channel (488 nm) with the other channels not shown.

Around 4 to 12 independent *Arabidopsis* seedlings were used for *Arabidopsis*-related root observation, and three leaves from three independent *N. benthamiana* plants were used for sensor-related confocal observation for each group in one experiment set. All the results were repeated for at least two times.

Pathogen infection assays

P. parasitica strain Pp016 (GFP tagged) or Pp042 was used for infection. Pathogens were cultured and inoculated as previously described: Plants were inoculated with 2000 zoospores for *P. parasitica* on *N. benthamiana* (*19*).

Gene expression assays

Total plant RNA was extracted using TRIzol reagent (Invitrogen), and 800 ng was reverse-transcribed into cDNA using the PrimeScript RT Reagent Kit with gDNA Eraser (Perfect for Real Time) (TakaRa).

Real-time qPCR (RT-qPCR) was performed using Ultra SYBR Mixture (CWBIO) with specific primers in a LightCycler 480 (Roche) under the following conditions: 95°C for 10 min and 50 cycles of 95°C for 15 s and 60°C for 30 s. Relative gene expression levels were calculated using the $2^{-\Delta\Delta Ct}$ method normalized with the reference genes *PpUBC9* for *P. parasitica*, *AtUBC9* for *Arabidopsis*, and *NbEF1α* for *N. benthamiana*. For RT-PCR, target genes were amplified for 28 cycles using EasyTaq DNA polymerase (TransGen Biotech). Primers are listed in table S1.

Statistical analysis

Data were analyzed using either a two-tailed Student's *t* test or analysis of variance (ANOVA) with Dunn's, Bonferroni's, or Tukey's post hoc tests or Brown-Forsythe ANOVA test with Dunnett's T3 post hoc test using Prism 9 (GraphPad). Statistical tests used for each panel are found in the corresponding legends.

Supplementary Materials

This PDF file includes:

Figs. S1 to S13
Table S1

REFERENCES AND NOTES

1. J. D. G. Jones, B. J. Staskawicz, J. L. Dangl, The plant immune system: From discovery to deployment. *Cell* **187**, 2095–2116 (2024).
2. H. Tian, Z. Wu, S. Chen, K. Ao, W. Huang, H. Yaghmaiean, T. Sun, F. Xu, Y. Zhang, S. Wang, X. Li, Y. Zhang, Activation of TIR signalling boosts pattern-triggered immunity. *Nature* **598**, 500–503 (2021).
3. R. N. Pruitt, F. Locci, F. Wanke, L. Zhang, S. C. Saile, A. Joe, D. Karelina, C. Hua, K. Fröhlich, W.-L. Wan, M. Hu, S. Rao, S. C. Stolze, A. Harzen, A. A. Gust, K. Harter, M. H. A. J. Joosten, B. P. H. J. Thomma, J.-M. Zhou, J. L. Dangl, D. Weigel, H. Nakagami, C. Oecking, F. E. Kasmi, J. E. Parker, T. Nürnberger, The EDS1–PAD4–ADR1 node mediates *Arabidopsis* pattern-triggered immunity. *Nature* **598**, 495–499 (2021).
4. B. P. M. Ngou, J. D. G. Jones, P. Ding, Plant immune networks. *Trends Plant Sci.* **27**, 255–273 (2022).
5. R. Mittler, S. I. Zandalinas, Y. Fichman, F. Van Breusegem, Reactive oxygen species signalling in plant stress responses. *Nat. Rev. Mol. Cell Biol.* **23**, 663–679 (2022).
6. Y. Fichman, S. I. Zandalinas, S. Peck, S. Luan, R. Mittler, HPCA1 is required for systemic reactive oxygen species and calcium cell-to-cell signaling and plant acclimation to stress. *Plant Cell* **34**, 4453–4471 (2022).
7. M. A. Torres, J. L. Dangl, J. D. G. Jones, Arabidopsis gp91phox homologues *AtrbohD* and *AtrbohF* are required for accumulation of reactive oxygen intermediates in the plant defense response. *Proc. Natl. Acad. Sci. U.S.A.* **99**, 517–522 (2002).
8. L. Li, M. Li, L. Yu, Z. Zhou, X. Liang, Z. Liu, G. Cai, L. Gao, X. Zhang, Y. Wang, S. Chen, J. M. Zhou, The FLS2-associated kinase BIK1 directly phosphorylates the NADPH oxidase RbohD to control plant immunity. *Cell Host Microbe* **15**, 329–338 (2014).
9. B. Wu, P. Li, X. Hong, C. Xu, R. Wang, Y. Liang, The receptor-like cytosolic kinase RIPK activates NADP-malic enzyme 2 to generate NADPH for fueling the ROS production. *Mol. Plant* **15**, 887–903 (2022).
10. F. Qi, J. Li, Y. Ai, K. Shangguan, P. Li, F. Lin, Y. Liang, DGK5β-derived phosphatidic acid regulates ROS production in plant immunity by stabilizing NADPH oxidase. *Cell Host Microbe* **32**, 425–440.e7 (2024).
11. L. Kong, X. Ma, C. Zhang, S.-I. Kim, B. Li, Y. Xie, I.-C. Yeo, H. Thapa, S. Chen, T. P. Devarenne, T. Munnik, P. He, L. Shan, Dual phosphorylation of DGK5-mediated PA burst regulates ROS in plant immunity. *Cell* **187**, 609–623.e21 (2024).
12. M. de Torres Zabala, G. Littlejohn, S. Jayaraman, D. Studholme, T. Bailey, T. Lawson, M. Tillich, D. Licht, B. Bolter, L. Delfino, W. Truman, J. Mansfield, N. Smirnoff, M. Grant, Chloroplasts play a central role in plant defence and are targeted by pathogen effectors. *Nat. Plants* **1**, 15074 (2015).
13. G. R. Littlejohn, S. Breen, N. Smirnoff, M. Grant, Chloroplast immunity illuminated. *New Phytol.* **229**, 3088–3107 (2021).
14. A. O. Nedo, H. Liang, J. Sriram, M. A. Razzak, J. Y. Lee, C. Kambhamettu, S. P. Dinesh-Kumar, J. L. Caplan, CHUP1 restricts chloroplast movement and effector-triggered immunity in epidermal cells. *New Phytol.* **244**, 1864–1881 (2024).
15. F. R. Palma, B. N. Gantner, M. J. Sakiyama, C. Kayzuka, S. Shukla, R. Lacchini, B. Cunniff, M. G. Bonini, ROS production by mitochondria: Function or dysfunction? *Oncogene* **43**, 295–303 (2023).
16. S. Marchi, E. Guilbaud, S. W. G. Tait, T. Yamazaki, L. Galluzzi, Mitochondrial control of inflammation. *Nat. Rev. Immunol.* **23**, 159–173 (2023).
17. M. Cvetkovska, G. C. Vanlerberghe, Coordination of a mitochondrial superoxide burst during the hypersensitive response to bacterial pathogen in *Nicotiana tabacum*. *Plant Cell Environ.* **35**, 1121–1136 (2012).
18. N. Yao, J. T. Greenberg, Arabidopsis ACCELERATED CELL DEATH2 modulates programmed cell death. *Plant Cell* **18**, 397–411 (2006).
19. Y. Yang, Y. Zhao, Y. Zhang, L. Niu, W. Li, W. Lu, J. Li, P. Schäfer, Y. Meng, W. Shan, A mitochondrial RNA processing protein mediates plant immunity to a broad spectrum of pathogens by modulating the mitochondrial oxidative burst. *Plant Cell* **34**, 2343–2363 (2022).
20. K. Khan, H. C. Tran, B. Mansuroglu, P. Önsell, S. Buratti, M. Schwarzländer, A. Costa, A. G. Rasmusson, O. Van Aken, Mitochondria-derived reactive oxygen species are the likely primary trigger of mitochondrial retrograde signaling in Arabidopsis. *Curr. Biol.* **34**, 327–342.e4 (2024).
21. P. Fuchs, F. Bohle, S. Lichtenauer, J. M. Ugalde, E. F. Araujo, B. Mansuroglu, C. Ruberti, S. Wagner, S. J. Muller-Schussele, A. J. Meyer, M. Schwarzlander, Reductive stress triggers ANAC017-mediated retrograde signaling to safeguard the endoplasmic reticulum by boosting mitochondrial respiratory capacity. *Plant Cell* **34**, 1375–1395 (2022).
22. H. Wu, P. Carvalho, G. K. Voeltz, Here, there, and everywhere: The importance of ER membrane contact sites. *Science* **361**, eaan5835 (2018).
23. D. Martinvalet, The role of the mitochondria and the endoplasmic reticulum contact sites in the development of the immune responses. *Cell Death Dis.* **9**, 336 (2018).
24. L. Barazzuol, F. Giamogante, T. Calì, Mitochondria associated membranes (MAMs): Architecture and physiopathological role. *Cell Calcium* **94**, 102343 (2021).
25. J. Loncke, A. Kaasik, I. Bezprozvanny, J. B. Parys, M. Kerkhofs, G. Bultynck, Balancing ER-mitochondrial Ca^{2+} fluxes in health and disease. *Trends Cell Biol.* **31**, 598–612 (2021).
26. M. Exposito-Rodriguez, P. P. Laissue, G. Yvon-Durocher, N. Smirnoff, P. M. Mullineaux, Photosynthesis-dependent H_2O_2 transfer from chloroplasts to nuclei provides a high-light signalling mechanism. *Nat. Commun.* **8**, 49 (2017).
27. I. M. Møller, Plant mitochondria and oxidative stress: electron transport, NADPH turnover, and metabolism of reactive oxygen species. *Annu. Rev. Plant. Physiol. Plant. Mol. Biol.* **52**, 561–591 (2001).
28. T. O. Bozkurt, S. Kamoun, The plant-pathogen haustorial interface at a glance. *J. Cell Sci.* **133**, jcs237958 (2020).
29. Y. Takahashi, Y. Uehara, T. Berberich, A. Ito, H. Saitoh, A. Miyazaki, R. Terauchi, T. Kusano, A subset of hypersensitive response marker genes, including *HSR203J*, is the downstream target of a spermine signal transduction pathway in tobacco. *Plant J.* **40**, 586–595 (2004).
30. M. Bonora, C. Morganti, G. Morciano, C. Giorgi, M. R. Wieckowski, P. Pinton, Comprehensive analysis of mitochondrial permeability transition pore activity in living cells using fluorescence-imaging-based techniques. *Nat. Protoc.* **11**, 1067–1080 (2016).
31. Y. Liao, M. Tian, H. Zhang, X. Li, Y. Wang, X. Xia, J. Zhou, Y. Zhou, J. Yu, K. Shi, D. Klessig, Salicylic acid binding of mitochondrial alpha-ketoglutarate dehydrogenase E2 affects mitochondrial oxidative phosphorylation and electron transport chain components and plays a role in basal defense against tobacco mosaic virus in tomato. *New Phytol.* **205**, 1296–1307 (2015).
32. S. K. Sanyal, P. Kanwar, J. L. Fernandes, S. Mahiwal, A. K. Yadav, H. Samtani, A. K. Srivastava, P. Suprasanna, G. K. Pandey, Arabidopsis mitochondrial voltage-dependent anion channels are involved in maintaining reactive oxygen species homeostasis, oxidative and salt stress tolerance in yeast. *Front. Plant Sci.* **11**, 50 (2020).
33. S. M. Lee, M. H. T. Hoang, H. J. Han, H. S. Kim, K. Lee, K. E. Kim, D. H. Kim, S. Y. Lee, W. S. Chung, Pathogen inducible voltage-dependent anion channel (AtVDAC) isoforms are localized to mitochondria membrane in arabidopsis. *Mol. Cells* **27**, 321–328 (2009).
34. N. Singh, B. Ravi, L. K. Saini, G. K. Pandey, Voltage-dependent anion channel 3 (VDAC3) mediates P. syringae induced ABA-SA signaling crosstalk in Arabidopsis thaliana. *Plant Physiol. Biochem.* **206**, 108237 (2024).
35. P. Kachroo, T. M. Burch-Smith, M. Grant, An emerging role for chloroplasts in disease and defense. *Annu. Rev. Phytopathol.* **59**, 423–445 (2021).
36. E. L. Robb, J. M. Gawel, D. Aksentijevic, H. M. Cocheme, T. S. Stewart, M. M. Shchepinova, H. Qiang, T. A. Prime, T. P. Bright, A. M. James, M. J. Shattock, H. M. Senn, R. C. Hartley, M. P. Murphy, Selective superoxide generation within mitochondria by the targeted redox cycler MitoParaquat. *Free Radic. Biol. Med.* **89**, 883–894 (2015).
37. M. P. Murphy, H. Bayir, V. Belousov, C. J. Chang, K. J. A. Davies, M. J. Davies, T. P. Dick, T. Finkel, H. J. Forman, Y. Janssen-Heininger, D. Gems, V. E. Kagan, B. Kalyanaraman, N.-G. Larsson, G. L. Milne, T. Nyström, H. E. Poulsen, R. Radi, H. Van Remmen, P. T. Schumacker, P. J. Thornalley, S. Toyokuni, C. C. Winterbourn, H. Yin, B. Halliwell, Guidelines for measuring reactive oxygen species and oxidative damage in cells and in vivo. *Nat. Metab.* **4**, 651–662 (2022).
38. I. Sorrentino, M. Galli, I. Medrano-Fernandez, R. Sitia, Transfer of H_2O_2 from Mitochondria to the endoplasmic reticulum via Aquaporin-11. *Redox Biol.* **55**, 102410 (2022).
39. S. Bestetti, M. Galli, I. Sorrentino, P. Pinton, A. Rimessi, R. Sitia, I. Medrano-Fernandez, Human aquaporin-11 guarantees efficient transport of H_2O_2 across the endoplasmic reticulum membrane. *Redox Biol.* **28**, 101326 (2020).
40. U. Johanson, M. Karlsson, I. Johansson, S. Gustavsson, S. Sjövall, L. Fraysse, A. R. Weig, P. Kjellbom, The complete set of genes encoding major intrinsic proteins in arabidopsis provides a framework for a new nomenclature for major intrinsic proteins in plants. *Plant Physiol.* **126**, 1358–1369 (2001).
41. L. Verdoucq, C. Maurel, "Chapter Two-Plant Aquaporins" in *Advances in Botanical Research*, C. Maurel, Ed. (Academic Press, 2018), vol. 87, pp. 25–56.
42. J. M. Ugalde, I. Aller, L. Kudrjasova, R. R. Schmidt, M. Schlößer, M. Homagk, P. Fuchs, S. Lichtenauer, M. Schwarzländer, S. J. Müller-Schüssele, A. J. Meyer, Endoplasmic reticulum oxidoreductin provides resilience against reductive stress and hypoxic conditions by mediating luminal redox dynamics. *Plant Cell* **34**, 4007–4027 (2022).
43. C. Lopez-Crisosto, A. Diaz-Vegas, P. F. Castro, B. A. Rothermel, R. Bravo-Sagua, S. Lavandero, Endoplasmic reticulum-mitochondria coupling increases during doxycycline-induced mitochondrial stress in HeLa cells. *Cell Death Dis.* **12**, 657 (2021).
44. M. G. Romei, S. G. Boxer, Split green fluorescent proteins: Scope, limitations, and outlook. *Annu. Rev. Biophys.* **48**, 19–44 (2019).
45. D. Vecellio Reane, R. Rizzuto, A. Raffaello, The ER-mitochondria tether at the hub of Ca^{2+} signaling. *Curr. Opin. Physio.* **17**, 261–268 (2020).

46. D. M. Booth, B. Enyedi, M. Geiszt, P. Varnai, G. Hajnoczky, Redox nanodomains are induced by and control calcium signaling at the ER-mitochondrial interface. *Mol. Cell* **63**, 240–248 (2016).
47. S. Koh, A. André, H. Edwards, D. Ehrhardt, S. Somerville, *Arabidopsis thaliana* subcellular responses to compatible *Erysiphe cichoracearum* infections. *Plant J.* **44**, 516–529 (2005).
48. R. Fuchs, M. Kopischke, C. Klapprodt, G. Hause, A. J. Meyer, M. Schwarzlander, M. D. Fricker, V. Lipka, Immobilized subpopulations of leaf epidermal mitochondria mediate PENETRATION2-dependent pathogen entry control in arabidopsis. *Plant Cell* **28**, 130–145 (2016).
49. G. Fan, Y. Yang, T. Li, W. Lu, Y. Du, X. Qiang, Q. Wen, W. Shan, A *Phytophthora capsici* RXLR effector targets and inhibits a plant PPIase to suppress endoplasmic reticulum-mediated immunity. *Mol. Plant* **11**, 1067–1083 (2018).
50. S. Altenhöfer, P. W. M. Kleikers, K. A. Radermacher, P. Scheurer, J. J. Rob Hermans, P. Schiffers, H. Ho, K. Wingler, H. H. H. W. Schmidt, The NOX toolbox: Validating the role of NADPH oxidases in physiology and disease. *Cell. Mol. Life Sci.* **69**, 2327–2343 (2012).
51. K. Hirano, W. S. Chen, A. L. W. Chueng, A. A. Dunne, T. Seredenina, A. Filippova, S. Ramachandran, A. Bridges, L. Chaudry, G. Pettman, C. Allan, S. Duncan, K. C. Lee, J. Lim, M. T. Ma, A. B. Ong, N. Y. Ye, S. Nasir, S. Mulyanidewi, C. C. Aw, P. P. Oon, S. Liao, D. Li, D. G. Johns, N. D. Miller, C. H. Davies, E. R. Browne, Y. Matsuoka, D. W. Chen, V. Jaquet, A. R. Rutter, Discovery of GSK2795039, a novel small molecule NADPH oxidase 2 inhibitor. *Antioxid. Redox Signal.* **23**, 358–374 (2015).
52. B. Kornmann, E. Currie, S. R. Collins, M. Schuldiner, J. Nunnari, J. S. Weissman, P. Walter, An ER-mitochondria tethering complex revealed by a synthetic biology screen. *Science* **325**, 477–481 (2009).
53. S. H. Howell, Endoplasmic reticulum stress responses in plants. *Annu. Rev. Plant Biol.* **64**, 477–499 (2013).
54. X. Qiang, B. Zechmann, M. U. Reitz, K. H. Kogel, P. Schafer, The mutualistic fungus *Piriformospora indica* colonizes *Arabidopsis* roots by inducing an endoplasmic reticulum stress-triggered caspase-dependent cell death. *Plant Cell* **24**, 794–809 (2012).
55. X. Qiang, X. Liu, X. Wang, Q. Zheng, L. Kang, X. Gao, Y. Wei, W. Wu, H. Zhao, W. Shan, Susceptibility factor RTP1 negatively regulates *Phytophthora parasitica* resistance via modulating UPR regulators bZIP60 and bZIP28. *Plant Physiol.* **186**, 1269–1287 (2021).
56. Y. Wakasa, Y. Oono, T. Yazawa, S. Hayashi, K. Ozawa, H. Handa, T. Matsumoto, F. Takaiwa, RNA sequencing-mediated transcriptome analysis of rice plants in endoplasmic reticulum stress conditions. *BMC Plant Biol.* **14**, 101 (2014).
57. Y. Saijo, N. Tintor, X. Lu, P. Rauf, K. Pajerowska-Mukhtar, H. Häweker, X. Dong, S. Robatzek, P. Schulze-Lefert, Receptor quality control in the endoplasmic reticulum for plant innate immunity. *EMBO J.* **28**, 3439–3449 (2009).
58. V. Nekrasov, J. Li, M. Batoux, M. Roux, Z.-H. Chu, S. Lacombe, A. Rougon, P. Bittel, M. Kiss-Papp, D. Chinchilla, H. P. van Esse, L. Jorda, B. Schwessinger, V. Nicaise, B. P. H. J. Thomma, A. Molina, J. D. G. Jones, C. Zipfel, Control of the pattern-recognition receptor EFR by an ER protein complex in plant immunity. *EMBO J.* **28**, 3428–3438 (2009).
59. Y. Wang, K. Bouwmeester, J. E. van de Mortel, W. Shan, F. Govers, A novel Arabidopsis-oomycete pathosystem: Differential interactions with *Phytophthora capsici* reveal a role for camalexin, indole glucosinolates and salicylic acid in defence. *Plant Cell Environ.* **36**, 1192–1203 (2013).
60. Y. Yang, "Negative regulation of plant immunity by mitochondiral RNA processing factors RTP7 and MORF8 to *Phytophthora*," thesis, Northwest A&F University, China, 2022.
61. D. Arnaud, M. J. Deeks, N. Smirnoff, Organelle-targeted biosensors reveal distinct oxidative events during pattern-triggered immune responses. *Plant Physiol.* **191**, 2551–2569 (2023).
62. R. Ozgur, B. Uzilday, A. H. Sekmen, I. Turkan, The effects of induced production of reactive oxygen species in organelles on endoplasmic reticulum stress and on the unfolded protein response in arabidopsis. *Ann. Bot.* **116**, 541–553 (2015).
63. X. Meng, L. Li, I. De Clercq, R. Narsai, Y. Xu, A. Hartmann, D. L. Claros, E. Custovic, M. G. Lewsey, J. Whelan, O. Berkowitz, ANAC017 coordinates organellar functions and stress responses by reprogramming retrograde signaling. *Plant Physiol.* **180**, 634–653 (2019).
64. Z. Zheng, S. A. Qamar, Z. Chen, T. Mengiste, Arabidopsis WRKY33 transcription factor is required for resistance to necrotrophic fungal pathogens. *Plant J.* **48**, 592–605 (2006).
65. J. Wang, G. Xu, Y. Ning, X. Wang, G.-L. Wang, Mitochondrial functions in plant immunity. *Trends Plant Sci.* **27**, 1063–1076 (2022).
66. M. Á. Peláez-Vico, Y. Fichman, S. I. Zandalinas, F. Van Breusegem, S. M. Karpiński, R. Mittler, ROS and redox regulation of cell-to-cell and systemic signaling in plants during stress. *Free Radicals Biol. Med.* **193**, 354–362 (2022).
67. I. Shiiba, N. Ito, H. Oshio, Y. Ishikawa, T. Nagao, H. Shimura, K.-W. Oh, E. Takasaki, F. Yamaguchi, R. Konagaya, H. Kadowaki, H. Nishitoh, T. Tanzawa, S. Nagashima, A. Sugiura, Y. Fujikawa, K. Umezawa, Y. Tamura, B. Il Lee, Y. Hirabayashi, Y. Okazaki, T. Sawa, R. Inatome, S. Yanagi, ER-mitochondria contacts mediate lipid radical transfer via RMDN3/PTPIP51 phosphorylation to reduce mitochondrial oxidative stress. *Nat. Commun.* **16**, 1508 (2025).
68. X. Zhang, R. Henriques, S. S. Lin, Q. W. Niu, N. H. Chua, *Agrobacterium*-mediated transformation of *Arabidopsis thaliana* using the floral dip method. *Nat. Protoc.* **1**, 641–646 (2006).
69. P. Varnai, B. Thyagarajan, T. Rohacs, T. Balla, Rapidly inducible changes in phosphatidylinositol 4,5-bisphosphate levels influence multiple regulatory functions of the lipid in intact living cells. *J. Cell Biol.* **175**, 377–382 (2006).
70. D. R. J. Verboogen, N. González Mancha, M. ter Beest, G. van den Bogaart, Fluorescence lifetime imaging microscopy reveals rerouting of SNARE trafficking driving dendritic cell activation. *eLife* **6**, e23525 (2017).
71. J.-G. Lee, S. Takahama, G. Zhang, S. I. Tomarev, Y. Ye, Unconventional secretion of misfolded proteins promotes adaptation to proteasome dysfunction in mammalian cells. *Nat. Cell Biol.* **18**, 765–776 (2016).
72. D. G. Millar, G. C. Shore, The signal anchor sequence of mitochondrial Mas70p contains an oligomerization domain. *J. Biol. Chem.* **268**, 18403–18406 (1993).
73. G. B. Waypa, J. D. Marks, R. Guzy, P. T. Mungai, J. Schriewer, D. Dokic, P. T. Schumacker, Hypoxia triggers subcellular compartmental redox signaling in vascular smooth muscle cells. *Circ. Res.* **106**, 526–535 (2010).
74. B. Morgan, K. Van Laer, T. N. Owusu, D. Ezerina, D. Pastor-Flores, P. S. Amponsah, A. Tursch, T. P. Dick, Real-time monitoring of basal H_2O_2 levels with peroxiredoxin-based probes. *Nat. Chem. Biol.* **12**, 437–443 (2016).
75. I. Aller, N. Rouhier, A. J. Meyer, Development of roGFP2-derived redox probes for measurement of the glutathione redox potential in the cytosol of severely glutathione-deficient rml1 seedlings. *Front. Plant Sci.* **4**, 506 (2013).
76. Y. Yang, G. Fan, Y. Zhao, Q. Wen, P. Wu, Y. Meng, W. Shan, Cytidine-to-Uridine RNA editing factor NbMORF8 negatively regulates plant immunity to *Phytophthora* pathogens. *Plant Physiol.* **184**, 2182–2198 (2020).
77. M. Senthil-Kumar, K. S. Mysore, Tobacco rattle virus-based virus-induced gene silencing in *Nicotiana benthamiana*. *Nat. Protoc.* **9**, 1549–1562 (2014).
78. J. Niemeyer, D. Scheuring, J. Oestreicher, B. Morgan, M. Schroda, Real-time monitoring of subcellular H_2O_2 distribution in *Chlamydomonas reinhardtii*. *Plant Cell* **33**, 2935–2949 (2021).
79. E. Park, H. Y. Lee, J. Woo, D. Choi, S. P. Dinesh-Kumar, Spatiotemporal monitoring of *Pseudomonas* effectors via type III secretion using split fluorescent protein fragments. *Plant Cell* **29**, 1571–1584 (2017).
80. A. P.-T. Jost, J. C. Waters, Designing a rigorous microscopy experiment: Validating methods and avoiding bias. *J. Cell Biol.* **218**, 1452–1466 (2019).

Acknowledgments: We thank M. Zhang (Shaanxi Normal University) for the *rbohD/F* double-mutant seeds; Z. Ma (College of Agronomy, Northwest A&F University), Y. Li, and Z. Bai (College of Plant Protection, Northwest A&F University) for the technical support with confocal microscopes; and G. Pei and M. Huo (SKLCSRHEP, Northwest A&F University) in supporting transmission electron microscopy. **Funding:** This work was supported by China Agriculture Research System CARS-09 (to W.S.), the Postdoctoral Science Foundation of China #GZB20230598 (to Y.Y.), the National Natural Science Foundation of China #32300263 (to Y.Y.), the National Natural Science Foundation of China #31930094 and #31125022 (to W.S.), and the Program of Introducing Talents of Innovative Discipline to Universities from the State Administration for Foreign Experts Affairs P. R. China #B18042 (to W.S.). **Author contributions:** Conceptualization: Y.Y., W.S., M.G.. Methodology: Y.Y., W.S.. Investigation: Y.Y., Y. Zhao, W.Z., and H.W. Resources: W.S., Y.Y., Y. Zhao, H.W., Y. Zhang, and Y.M. Validation: W.S., Y.Y., Y. Zhao, W.Z., H.W., and Y.M. Data curation: W.S., Y.Y., W.Z., and Y.M. Formal analysis: Y.Y. Visualization: Y.Y. Funding acquisition: Y.Y. and W.S. Project administration: W.S. and Y.M. Supervision: W.S. Writing—original draft: Y.Y., W.S., M.G., and P.S. Writing—review and editing: W.S., Y.Y., M.G., Y. Zhang, P.S., and Y.M. **Competing interests:** W.S. and Y.Y. are inventors of two patents (ZL202010237638.2 and US 11,920,143B2) that cover the *RTP7* in *Arabidopsis* and *N. benthamiana* and filed by Northwest A&F University. W.S., Y.Y., and Y.M. are inventors on one patent (ZL202211459529.0) that covers the *RTP7* in potato and filed by Northwest A&F University. All other authors declare that they have no competing interests. **Data and materials availability:** Genes described here in the following The Arabidopsis Information Resource (www.arabidopsis.org/) gene accession numbers: *AtRTP7* (AT4G02820), *RBOHD* (AT5G47910), *RBOHF* (AT1G64060), *VDAC3* (At5G15090), *Atnad7* (ATMG00510), *AtERO1* (AT1G72280), *AtERO2* (AT2G38960), and *AtSIP1;1* (At3G04090). The following identifiers are used for *N. benthamiana* loci from the Sol Genomics Network (https://solgenomics.net/): *NbRTP7* (Niben101Scf00317g06017.1; https://solgenomics.net/tools/blast/match/show?blast_db_id=266;id=Niben101Scf00317g06017.1), *NbEROs* (Niben101Scf04377g01001.1, Niben101Scf04225g02006.1, Niben101Scf00885g14013.1, and Niben101Scf01042g02007.1, with following links: https://solgenomics.net/tools/blast/match/show?blast_db_id=266;id=Niben101Scf04377g01001.1, https://solgenomics.net/tools/blast/match/show?blast_db_id=266;id=Niben101Scf04225g02006.1, https://solgenomics.net/tools/blast/match/show?blast_db_id=266;id=Niben101Scf00885g14013.1, and https://solgenomics.net/tools/blast/match/show?blast_db_id=266;id=Niben101Scf01042g02007.1), *NbSIP1s* (Niben101Scf03279g01001.1, Niben101Scf07155g03020.1, Niben101Scf23427g00004.1, and Niben101Scf00801g00012.1, with following links: https://solgenomics.net/tools/blast/match/show?blast_db_id=266;id=Niben101Scf03279g01001.1, https://solgenomics.net/tools/

blast/match/show?blast_db_id=266;id=Niben101Scf07155g03020.1, https://solgenomics.net/tools/blast/match/show?blast_db_id=266;id=Niben101Scf23427g00004.1, and https://solgenomics.net/tools/blast/match/show?blast_db_id=266;id=Niben101Scf00801g00012.1), and *NbSIP2s* (Niben101Scf03757g03002.1 and Niben101Scf13391g01005.1, with following links: https://solgenomics.net/tools/blast/match/show?blast_db_id=266;id=Niben101Scf03757g03002.1 and https://solgenomics.net/tools/blast/match/show?blast_db_id=266;id=Niben101Scf13391g01005.1). *NbVDACs* (MW367440.1, MW367441.1, MW367442.1, and MW367443.1) in GeneBank. All other data needed to evaluate the conclusions in the paper are present in the paper and/or the Supplementary Materials.

Submitted 11 May 2025
Accepted 5 September 2025
Published 1 October 2025
10.1126/sciadv.ady9234